

## Numerical Investigations of Flow Field over Conical, Disc and Flat-Face Spiked-Nose Attached to a Hemisphere Body at Mach 6

R. C. Mehta<sup>1\*</sup>

<sup>1</sup>Department of Aeronautical Engineering, Noorul Islam Centre for Higher Education, Kumaracoil 629180, India

DOI: [10.36347/sjet.2024.v12i07.001](https://doi.org/10.36347/sjet.2024.v12i07.001)

| Received: 27.05.2024 | Accepted: 03.07.2024 | Published: 05.07.2024

\*Corresponding author: R. C. Mehta

Department of Aeronautical Engineering, Noorul Islam Centre for Higher Education, Kumaracoil 629180, India

### Abstract

### Original Research Article

A forward-facing spike attached to a hemispherical body significantly alters its flow field and influences aerodynamic drag at high-speed flow. Consequently, the geometry, that is, the length and shape of the spike, has to be investigated in order to obtain a large conical recirculation region in front of the hemispherical body to get beneficial drag reduction. It is, therefore, a potential candidate for aerodynamic drag reduction for a future high-speed spiked hemispherical body. Axisymmetric compressible time-dependent Navier-Stokes equations are solved employing a finite volume discretization in conjunction with a multistage Runge-Kutta time stepping scheme. The effects of the spike length and shape, and the spike nose configuration on the reduction of drag are numerically evaluated at Mach 6 at a zero angle of incidence. Semi-cone angle of conical spike varied from  $10^\circ$  to  $30^\circ$  are to get the different type of flow field such as formation of conical shock wave, separation region and reattachment of shock wave are analyzed in conjunction with flat-disk spike and hemispherical disk spike attached to the hemispherical body. The bow shock distance ahead of the hemispherical and flat-disc is compared with the analytical solution and good agreement found between them. The influence of the reattachment shock wave generated from different spike shape are is used to understand the cause of drag reduction fluid mechanics.

**Keywords:** Aerodynamic drag; Computational fluid dynamics; Viscous flow; Hypersonic flow; Shock wave.

Copyright © 2024 The Author(s): This is an open-access article distributed under the terms of the Creative Commons Attribution 4.0 International License (CC BY-NC 4.0) which permits unrestricted use, distribution, and reproduction in any medium for non-commercial use provided the original author and source are credited.

## INTRODUCTION

High-speed flow past a hemispherical body generates a bow shock wave which causes high surface pressure and as a result the development of high aerodynamic drag. The dynamic pressure on the surface of the blunt body can be significantly reduced by creating a low-pressure region in front of the hemispherical body by attaching a spike. It is advantageous to have a vehicle with a low drag coefficient in order to minimize the thrust required from the propulsive system during the supersonic and hypersonic regime.

Experimental investigations of the flow field around a spiked-blunt body were started in the 1940s. The prime focus was with regard to drag characteristics where effects due to spike length, spike head geometry, forward body geometry and relative spike diameter have been explored. Most of the experimental studies on spiked bodies are carried out to get effects on flow field [1-5] at supersonic and hypersonic Mach numbers [6-9]. Kubota [10] has experimentally investigated the overall characteristics of the spiked blunt body configuration at hypersonic Mach numbers. Crawford [11]

experimentally investigated the effects of the spike length on the nature of the flow field for a Mach 6.8 and Reynolds number  $0.12 \times 10^6 - 1.5 \times 10^6$  based on the cylinder diameter. The spike drastically changes the aerodynamic drag of the hemisphere body at high-speeds. Attributed to the reattachment of the shear layer on the shoulder of the hemispherical body, the pressure near that reattachment point becomes large. Motoyama *et al.*, [12] have experimentally investigated the aerodynamic characteristics of conical, hemispherical, flat-faced aerospikes, and hemispherical and flat-faced disk attached to the aerospikes for a Mach 7, Reynolds number  $4 \times 10^5/m$ , for  $L/D = 0.5$  and  $1.0$ , and angle of attack  $0^\circ$  to  $8^\circ$ , where  $L$  is the spike length and  $D$  is the cylinder diameter. They found that the aerodisk spike ( $L/D = 1.0$  and aerodisk diameter of  $D_s = 10$  mm), has a superior drag reduction capability as compared to the other aerospikes. Yamauchi *et al.*, [13] have numerically investigated the flow field around a spiked blunt body at Mach numbers of 2.01, 4.14 and 6.80 for different ratio of  $L/D$ . Shoemaker [14], Fujita and Kubota [15], Boyce *et al.*, [16] have used a numerical approach to solve the compressible Navier-Stokes equations. Milicev *et al.*,

[17] have experimentally investigated the influence of four different types of spikes attached to a hemisphere-cylinder body at Mach 1.89, Reynolds number  $0.38 \times 10^6$  based on the cylinder diameter, and at an angle of incidence  $2^\circ$ . Numerical simulations [18] have been

carried out to get the comparative studies of the flowfield over the spike. Axisymmetric numerical simulation [19] has been performed for different types of spikes attached to a blunt nose cone at Mach 5.0, 7.0 and 10.0 using commercial flow solver CFD-FASTRAN.

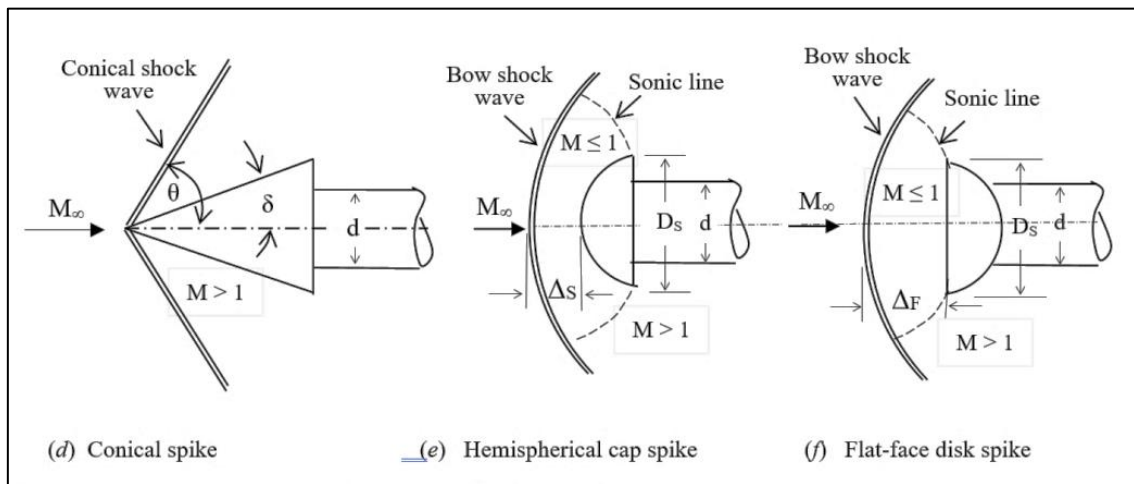
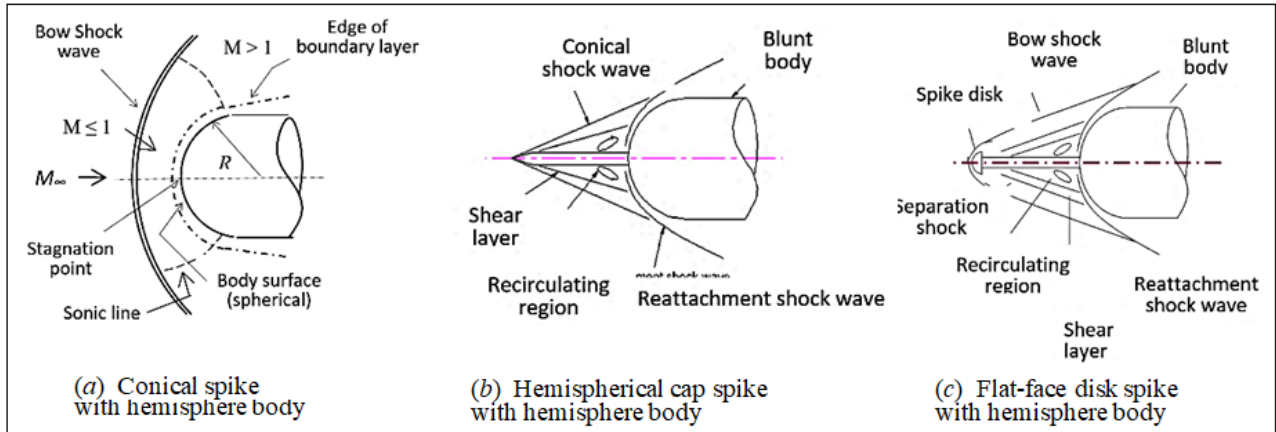


**Fig 1: Flow field over (a) without and with forward facing spike attached to hemisphere body (b) close-up view of the spike**

A schematic of the flow field over a hemisphere body, a conical and an aero-disk spiked attached to the hemisphere body at zero angle of attack is illustrated in Fig 1(a), (b) and (c), respectively. A bow shock is formed ahead of the hemisphere body as shown in Fig 1(a). Sonic line appears on the shoulder of the hemisphere body. Directly in front of the body an essentially normal shock is formed which extends around body as a curved oblique shock. A sufficient distance away from the body, the aerodynamic field is unaffected by the presence of the body. The strength of the shock decays continuously from its maximum value at the normal shock to a minimum strength or a Mach wave at infinity.

The flow field around a conical spike and a hemisphere disc shape spiked attached to the hemisphere body appears to be more complicated and complex and contains a number of interesting flow phenomena and characteristic, which has to be analyzed as illustrated in

Fig. 1(b) and 1(d). The re-circulating region is formed around the root of a spike up to the reattachment point of the flow at the shoulder of the hemispherical body. Due to the re-circulating region, the pressure at the stagnation region of the blunt body will decrease. The flow past the spike creates a conical shock wave which remains away from the body as depicted in Fig 1(b). One of the tools that has been used for study in conventional, perfect gas dynamics is the shock-polar diagram. Although this diagram can be used for quantitative analysis and occasionally has been so employed, it primarily serves to complement perfect gas flow tables by providing a graphical display of the velocity vectors and wave geometry for all of the possible oblique shock wave solutions pertaining to a given freestream condition. Flow behind the conical shock wave separates on the spike and create a conical shaped recirculation zone appears in the vicinity of the stagnation region. Due to the formation of the flow recirculation, the surface

pressure reduces in the forward-facing region of the hemisphere body. However, the reattachment of the shear layer on the shoulder of the hemispherical body increases surface pressure.

A bow shock wave is formed ahead of the spherical disc spike as illustrated in Fig. 1(c). The reattachment shock is moved downstream as shown in the Fig. 1(c), which is function of the geometrical parameter of the spike, i.e., the hemispherical disc spike. Enlarged view of the flow field over the conical shape spike, hemisphere disc shape spike and flat-face disc spike are delineated in Fig 1 (d), (e) and (f), respectively. The conical shock wave is emanating from the conical spike tip and impinging on the blunt body.

The main focus of the present paper is to calculate surface pressure and skin friction distributions, and aerodynamic drag over a forward-facing spike of

various shape and size at Mach 6. The present paper presents a numerical simulation of the flow field over a flat-face spike, hemispherical spike and conical spike for different  $L/D$  ratios. The semi-cone angle  $\delta$  of the conical spike is varied from  $10^\circ$  to  $30^\circ$ . The flow field features captured by the density, Mach and pressure contours are used to understand the mechanism of the drag reduction. The influence of the spike shock wave generated from the spike, interacting with the reattachment shock is also studied, to understand the cause of drag reduction.

**Governing Fluid dynamics Equations**

A numerical simulation of the time-dependent, compressible, axisymmetric Navier-Stokes equations is employed to numerically solve the basic fluid dynamics over a forward-facing spike attached to a hemisphere body. The governing equations can be written in the following strong conservation form:

$$\frac{\partial U}{\partial t} + \frac{\partial F}{\partial x} + \frac{\partial G}{\partial r} + H = \left[ \frac{\partial R}{\partial x} + \frac{\partial S}{\partial r} \right] \dots\dots\dots (1)$$

Where,

$$U = r \begin{bmatrix} \rho \\ \rho u \\ \rho v \\ \rho e \end{bmatrix}, F = r \begin{bmatrix} \rho u \\ \rho u^2 + p \\ \rho uv \\ (\rho e + p)u \end{bmatrix}, G = r \begin{bmatrix} \rho v \\ \rho uv \\ \rho v^2 + p \\ (\rho e + p)v \end{bmatrix} \dots\dots\dots (2)$$

Where  $U$  is conservative state and  $F$  and  $G$  are inviscid flux vectors;  $x$  and  $r$  are axial and radial coordinate system and  $t$  is time. The viscous flux vectors are

$$R = r \begin{bmatrix} 0 \\ \sigma_{xx} \\ \tau_{xr} \\ u\sigma_{xx} + v\tau_{xr} + q_x \end{bmatrix}, S = r \begin{bmatrix} 0 \\ \tau_{xx} \\ \sigma_{xr} \\ u\tau_{xr} + v\sigma_{rr} + q_r \end{bmatrix}, H = \begin{bmatrix} 0 \\ 0 \\ \sigma_+ \\ 0 \end{bmatrix} \dots\dots\dots (3)$$

Where  $R$  and  $S$  are viscous flux vector and  $H$  is source vector,  $\sigma$  and  $\tau$  are components of the stress vector, while  $q$  is components of the heat flux vector. Thus, the viscous terms in the equations became:

$$\begin{aligned} \sigma_{xx} &= -\frac{2}{3}\mu \left( \nabla \cdot U + 2 \frac{\partial u}{\partial x} \right) \\ \sigma_{rr} &= -\frac{2}{3}\mu \left( \nabla \cdot U + 2 \frac{\partial v}{\partial r} \right) \\ \tau_{xr} &= \mu \left( \frac{\partial u}{\partial r} + \frac{\partial v}{\partial x} \right) \\ \sigma_+ &= -p - \mu \left( \frac{2}{3} \nabla \cdot U + 2 \frac{v}{r} \right) \dots\dots\dots (4) \\ \nabla \cdot U &= \frac{\partial u}{\partial x} + \frac{\partial v}{\partial r} + \frac{v}{r} \\ q_x &= -k \frac{\partial T}{\partial x} \\ q_r &= -k \frac{\partial T}{\partial r} \end{aligned}$$

Where  $k$  is thermal conductivity. The coefficient of molecular viscosity  $\mu$  is calculated according to Sutherland’s law

$$\mu = 1.458 \times 10^{-6} \frac{T^{1.5}}{T+110.4} \dots\dots\dots (5)$$

The temperature is related to pressure and density by perfect gas equation of state as

$$p = (\gamma - 1)\rho \left[ e - \frac{1}{2}(u^2 + v^2) \right] \dots\dots\dots (6)$$

The ratio of the specific heat  $\gamma$  is assumed constant and is equal to 1.4. The flow is assumed to be laminar, which is also consistent to Bogdonoff and Vas [1], Yamauchi *et al.*, [13], Fujita and Kubota [15], and Boyce *et al.*, [16].

$$\frac{\partial}{\partial t} \int_{\Omega} \mathbf{U} d\Omega + \int_{\Gamma} (\mathbf{F} dr - \mathbf{G} dx) = \int_{\Gamma} (\mathbf{R} dr - \mathbf{S} dx) - \int_{\Omega} \mathbf{H} d\Omega \dots\dots\dots (7)$$

Where  $\Omega$  is the computational domain,  $\Gamma$  is the boundary of the region. The contour integration around the boundary of the cell is taken in the anticlockwise sense. The flow field simulation employs a finite volume discretization technique. The spatial computation domain was divided into a finite number of non-overlapping quadrilateral cells. Figure 2 depicts a typical computational cell which has four vertices ( $a - d$ ). The conservation variables within the computational cell are represented by their average values at the cell centre. The spatial and temporal terms are decoupled using the method of lines. Thus, the discretized solution to the governing equations results in a set of volume-averaged state variables for mass, momentum, and energy, which are in balance with their area-averaged fluxes (inviscid and viscous) across the cell faces [20]. The cell used for gradient calculations forms a second mesh that is shifted a half cell in the axial and radial directions in relation to

$$A_{i,j} \frac{\partial U_{i,j}}{\partial t} + Q(U_{i,j}) - V(U_{i,j}) + D(U_{i,j}) + A_{i,j}(U_{i,j}) = 0 \dots\dots\dots (8)$$

Where  $A_{i,j}$  is the area of the computational cell,  $Q(U_{i,j})$  and  $V(U_{i,j})$  are inviscid and viscous fluxes respectively, and  $D(U_{i,j})$  is the artificial dissipation flux added for numerical stability.

**Artificial Dissipation**

In cell-centered spatial discretization schemes, such as above which is non-dissipative, therefore, artificial are added to Eq. (8). The approach of Jameson *et al.*, [21] is adapted to construct the dissipative function  $D_{i,j}$  consisting of a blend of second and fourth differences of the vector conserved variables  $U_{i,j}$ . Fourth differences are added everywhere in the flow domain where the solution is smooth, but are ‘switched-off’ in the region of shock waves. A term involving second differences is then ‘switch-on’ to damp oscillations in the vicinity of shock waves. This switching is achieved by means of a shock sensor based on the local second differences of pressure. Since the computational domain is having structured grids, the cell centers are defined by two indices ( $i,j$ ) in these coordinate directions. The dissipation term is written in terms of differences of cell-edge values as

$$D_{i,j} = \frac{\Delta A_{i,j}(d_{AB} - d_{CD} + d_{BC} - d_{DA})}{\Delta t_{i,j}} \dots\dots\dots (9)$$

Where  $\Delta t_{i,j}$  is the local cell-centre time step. The cell-edge components of the artificial dissipation terms are composed of first and second differences of dependent variables, e.g.

**Numerical algorithm**

To facilitate the spatial discretization in the numerical scheme, the time dependent axisymmetric compressible Navier-Stokes equations (1) can be written in the integral form over a finite volume as:

the original computational mesh. The derivatives  $\partial/\partial x$  and  $\partial/\partial r$  at the cell vertices ( $a' - d'$ ) can be determined by considering by auxiliary cells surrounding each side as shown in Fig. 2, where  $f$  stands for any of the primitive variables. The viscous flux vectors  $\mathbf{R}$  and  $\mathbf{S}$  are approximated in such a way as to preserve cell conservations and maintain algorithm simplicity. Figure 2 shows a typical stencil of the computing cell which has four edges ( $a - d$ ), four vortices and a cell-centre grid point  $A$ . The spatial and temporal terms are decoupled using the method of lines. The flux vector is divided into the inviscid and viscous components. A cell-centered scheme is used to store the flow variables. The discretization of inviscid fluxes is performed using the cell average scheme. When the integral governing Eq. (7) is applied separately to each cell in the computational domain, we obtain a set of coupled differential equations of the form:

$$d_{AB} = d_{AB}^{(2)} - d_{AB}^{(4)}$$

with

$$d_{AB}^{(2)} = \varepsilon_2^{(2)} (U_{i+1,j} - U_{i,j})$$

$$d_{AB}^{(4)} = \varepsilon_2^{(4)} (U_{i+2,j} - 3U_{i+1,j} + 3U_{i,j} - U_{i-1,j})$$

The adaptive coefficients

$$\varepsilon_2^{(2)} = \kappa^{(2)} \max(v_{i+1}, v_{i,j})$$

$$\varepsilon_2^{(4)} = \max(0, \kappa^{(4)} - \varepsilon_2^{(2)})$$

are switched on or off by use of the shock wave sensor  $v$ , with

$$v_{i,j} = \left| \frac{p_{i+1,j} - 2p_{i,j} + p_{i-1,j}}{p_{i+1,j} + 2p_{i,j} + p_{i-1,j}} \right| \dots\dots\dots (10)$$

Where  $\kappa^{(2)}$  and  $\kappa^{(4)}$  are constants, taken equal to 1/4 and 1/256 respectively. The scaling quantity  $[(\Delta A_{i,j})/(\Delta t_{i,j})]$  in Eq. (9) confirms the inclusion of the cell volume in the dependent variable. The blend of second and fourth differences provides third-order background dissipation in smooth regions of the flow and first-order dissipation at shock waves.

The spatial discretization can be summarized here which is employed in numerical simulations. The

convective terms are nonlinear, hyperbolic and grid dependent. A structured non-overlapping quadrilateral cell is used in the numerical simulations. The diffusive terms are quasi-linear, elliptic, grid independent, cell centered use of dual control volume for evaluating the gradients at a given location. Thus, the discretized solution to the governing equations results in a set of volume-averaged state variables of mass, momentum, and energy which are balance with their area-averaged fluxes (inviscid and viscous) across the cell faces. The finite volume code constructed in this manner reduces to a central difference scheme and is second-order accurate provided that the mesh is smooth enough. The cell-centered spatial discretization scheme is non-dissipative; therefore, artificial dissipation terms are included as a blend of a Laplacian and biharmonic operator in a manner analogous to the second and fourth difference. The artificial dissipation term was added explicitly to prevent numerical oscillations near the shock waves to damp high-frequency modes.

**Multi-stage Time-Stepping Scheme**

The spatial discretization described above reduces the governing flow equations to semi-discrete ordinary differential equations. The integration is performed employing an efficient multi-stage scheme. The following three-stage, time-stepping scheme is used for the numerical simulation (for clarity, the subscripts *i* and *j* are neglected here):

$$\begin{aligned}
 U^{(0)} &= U^n \\
 U^{(1)} &= U^n - 0.6\Delta t(R^{(0)} - D^{(0)}) \\
 U^{(2)} &= U^n - 0.6\Delta t(R^{(1)} - D^{(0)}) \dots\dots\dots(11) \\
 U^{(3)} &= U^n - 1.0\Delta t(R^{(2)} - D^{(0)}) \\
 U^{n+1} &= U^{(3)}
 \end{aligned}$$

Where *n* is the current time level, *n + 1* is the new time level, and residual *R* is the sum of the inviscid and viscous fluxes. The multi-stages time-stepping scheme has been proved to be second-order accurate in time for a linear system of one-dimensional equation. The artificial dissipation is evaluated only at the first stage. The permissible time step of an explicit scheme is limited by the Courant-Friedrichs-Lewy condition, which states that a difference scheme cannot be convergent and stable approximation unless its domain of dependence contains the domain of dependence of the corresponding differential equation. A conservative choice of the Courant number is made in the simulation to achieve a stable numerical solution. A global time-step is used rather than the grid-varying time-step to numerically simulate a time-accurate solution and is computed using following expression:

$$(\Delta t)_{i,j} = \min \left[ \frac{|u|}{\Delta x} + \frac{|v|}{\Delta r} + c \sqrt{\frac{1}{(\Delta x)^2 + (\Delta r)^2}} \right]^{-1} \dots (12)$$

Where grid points *i, j* are grid point as shown in Fig 2.

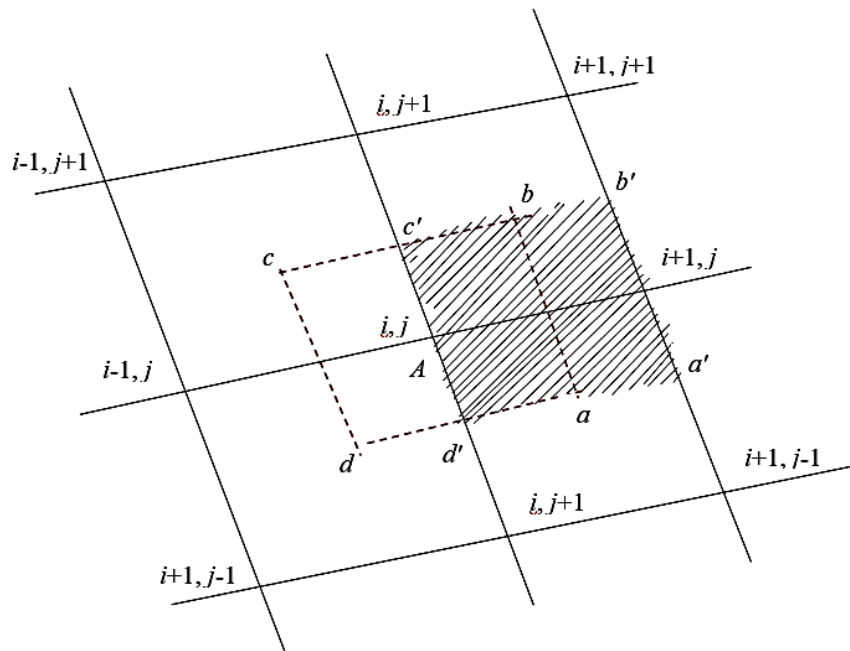


**Fig 2: Computational stencil employed in flow solver**

**Initial and boundary conditions**

Conditions corresponding to a Mach 6 were given as initial conditions. On the surface, no slip

condition is considered. An isothermal wall condition was prescribed for the surface of the model, that is, a wall temperature of 300° K. The symmetric conditions were

applied on the centerline. For supersonic flow, all the flow variables are extrapolated at the outflow from the vector of conservative vector,  $U$ .

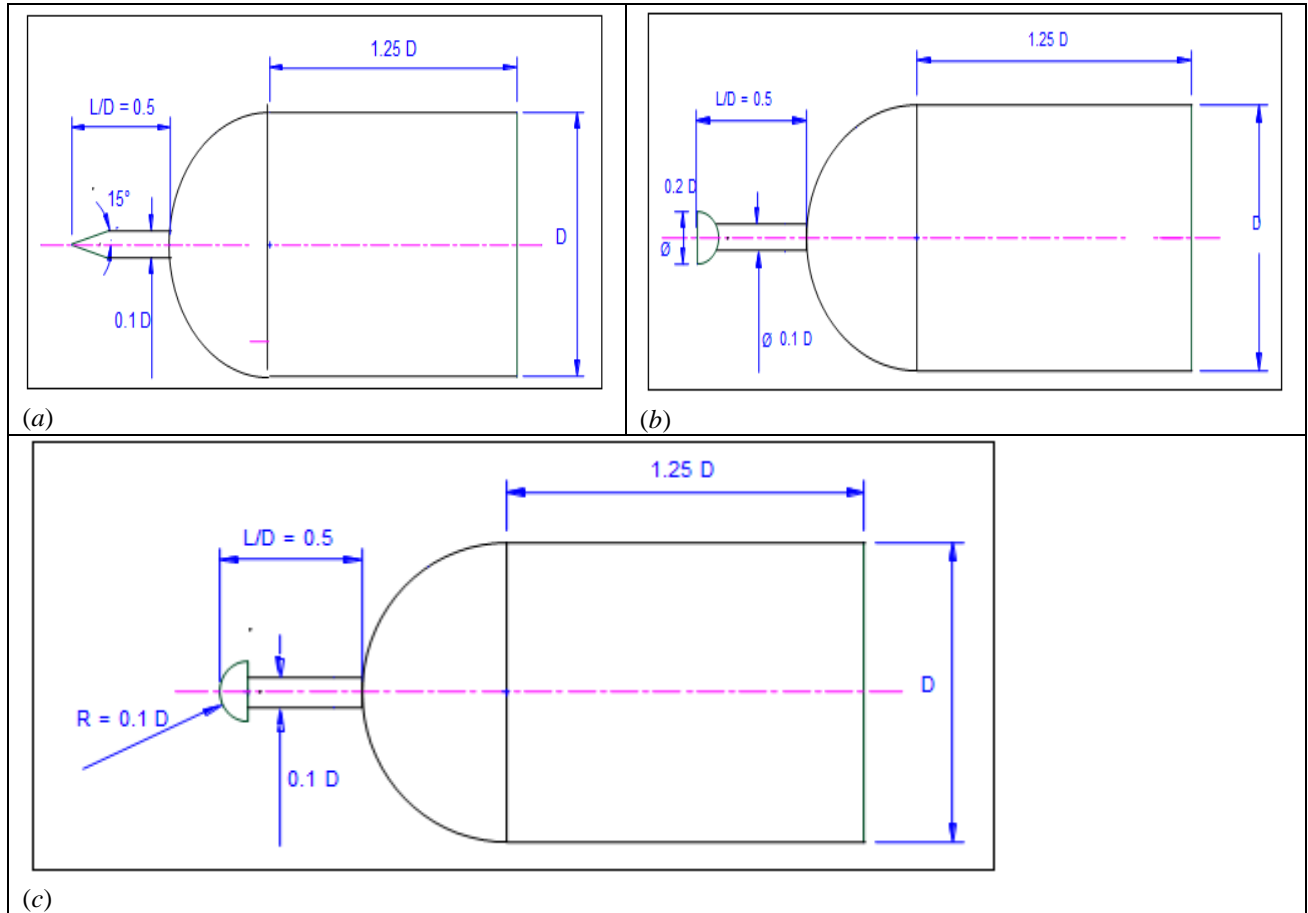


**Fig 3: Dimensions of the (a) conical spike (b) flat-face disc spike (c) hemispherical cap spike attached to the hemispherical blunt body**

**Spike Geometry**

The dimensions of the spiked hemisphere body considered in the present analysis are shown in Fig 3. The model is axisymmetric, the main body has a hemispherical-cylinder nose, and diameter  $D$  is  $4.0 \times 10^{-2}$  m. The spike consists of an aerodisc part and a cylindrical part. The diameter of the cylinder of the spike is  $0.1D$ . Spike having a hemispherical cap of radius  $0.1D$  attached with a sting of diameter of  $0.1D$ .

The spike consists of a conical part and a cylindrical part as shown in Fig. 3(a). The diameter of the cylinder of the spike is  $0.1 D$ . The angle of the semi-

cone cone is  $\delta = 15^\circ$  for the conical spike as shown in Fig. 3(c). Figure 3(b) shows the flat-face aerodisc. The spike length  $L = 0.5$  is simulated numerically. The aerodisc type spike configuration utilizes a disc on its nose of radius  $0.1D$  as shown in Fig. 3(c). The radius of the hemisphere aerodisk is  $0.05D$ . The diameter of the hemisphere aerodisk attached to the spike is that of the diameter of the spike-stem. In the numerical simulations, semi-cone angle  $\delta$  was varied from  $10^\circ$  to  $30^\circ$ . The spike lengths  $L = 0.5, 1.0$  and  $2.0 D$  are simulated numerically.

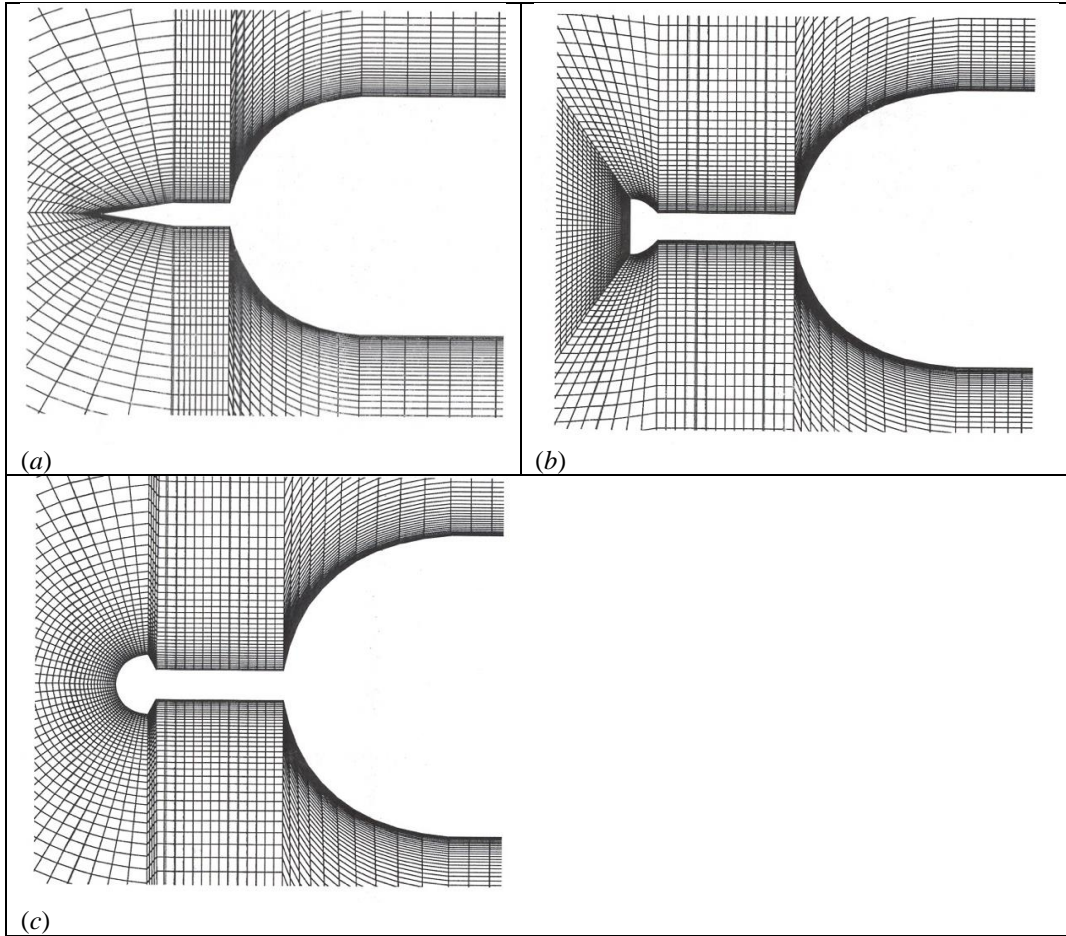


**Fig 4: Enlarged view of computational grid over (a) conical spike (b) flat-face disk spike and (c) hemispherical disk spike attached to the hemispherical blunt bod**

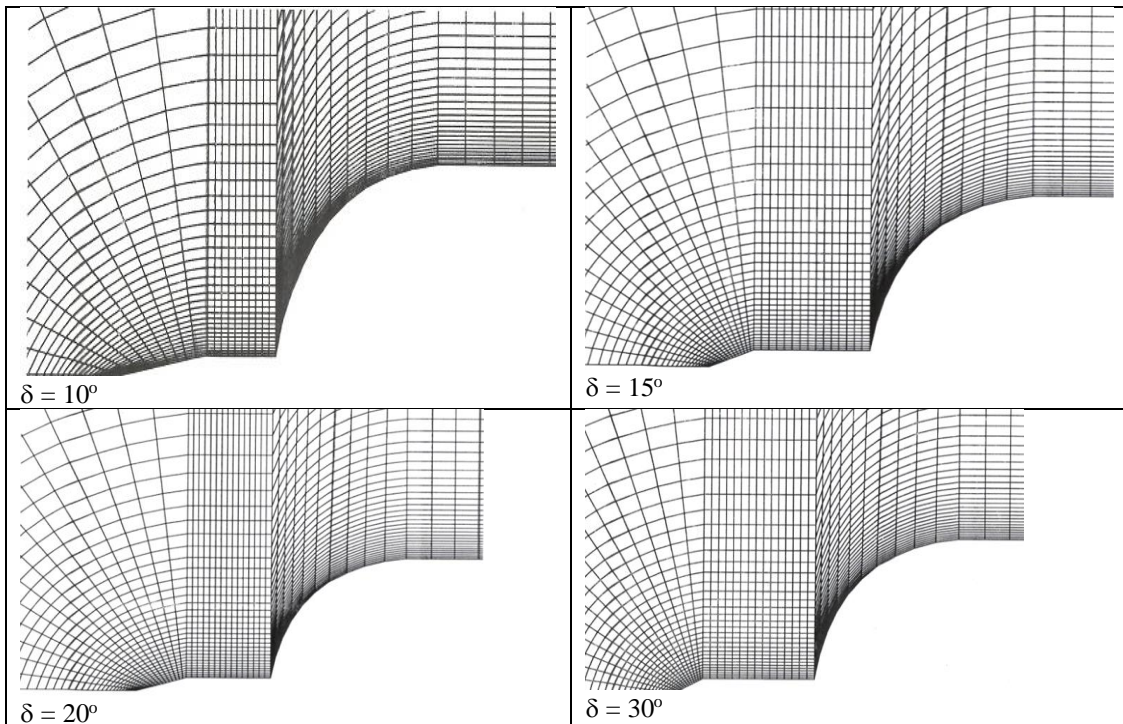


**Fig 5: Enlarged view of computational grid over a conical spike at semi-cone angle  $\delta = 10^\circ, 15^\circ, 20^\circ$  and  $30^\circ$  attached to a hemispherical blunt body**

**Grid Generation**

One of the controlling factors for the numerical simulation is the proper grid arrangement. The grid points are generated by a homotopy scheme [22]. The spiked hemisphere body is defined by a number of grid points in the cylindrical coordinate system. Using these surface points as the reference nodes, the normal coordinate is then described by the exponentially structured field points,  $(x_{i,j}, r_{i,j})$  extending outwards up to an outer computational boundary. Sufficient grid points are allotted in the shoulder region of the capsule. The stretching of grid points in the normal direction is obtained using the following expression. One of the controlling factors for the numerical simulation is the proper grid arrangement. Using these surface points as the reference nodes, the normal coordinate is then described by the exponentially structured field points,  $(x_{i,j}, r_{i,j})$  extending outwards up to an outer computational boundary. Sufficient grid points are allotted in the shoulder region of the capsule. The stretching of grid points in the normal direction is obtained using the following expression:

$$x_{i,j} = x_{i,0} \left[ \frac{e^{\frac{(j-1)\beta}{nr-1}} - 1}{e^{\beta} - 1} \right] + x_{i,w} \left[ \frac{e^{\frac{(j-1)\beta}{nr-1}} - 1}{e^{\beta} - 1} \right] \dots\dots\dots (13)$$

$$r_{i,j} = r_{i,0} \left[ \frac{e^{\frac{(j-1)\beta}{nr-1}} - 1}{e^{\beta} - 1} \right] + r_{i,w} \left[ \frac{e^{\frac{(j-1)\beta}{nr-1}} - 1}{e^{\beta} - 1} \right]$$

$i = 1, 2, 3, \dots, nx$   
 $j = 1, 2, 3, \dots, nr$

Where  $r_{i,w}$  and  $r_{i,0}$  are the wall and outer surface points, respectively, and  $\beta$  is a stretching factor.  $nx$  and  $nr$  are the total number of grid points in the  $x$  and  $r$  directions, respectively. Grid independent tests were carried out, taking into consideration the effect of the computational domain, the stretching factor to control the grid intensity near the wall, and the number of grid points in the axial and normal directions. The outer boundary of the computational domain is varied from 2.5 to 3.0 times the cylinder diameter  $D$  and the grid-stretching factor in the radial direction is varied from 1.5 to 5. These stretched grids are generated in an orderly manner. To verify the chosen grid delivers an accurate solution, the number of grid cells was increased until a steady state solution occurred, that is, the resulting axial

force on the investigated shape did not change anymore. Several test runs were made with a total doubled grid cell number. Therefore, the grid was highly refined in both directions. Grids are chosen with the number of grid points in the  $i$ -direction ranging from 187 for the shortest blunt spike to up to 220 for the longest spike configuration, and the number in the  $j$  direction ranging from 52 to 82. The present numerical analysis was performed on  $187 \times 62$  grid points. The downstream boundary of the computational domain is maintained at 4 to 6 times the cylinder diameter. This grid arrangement is found to give a relative difference of about  $\pm 1.5\%$  for the drag coefficient. The convergence criterion less than the  $10^{-5}$  is based on the difference in the density values at any grid point between two successive iterations. The minimum spacing for the fine mesh is dependent upon the Reynolds number and is calculated by  $\Delta r = (\frac{2}{3})D\sqrt{Re_D}$ . The finer mesh near the wall helps to resolve the viscous effects. The finer mesh near the wall helps to resolve the viscous effects.

A close-up view of the computational grid over the hemispherical, the conical, and the flat-faced aerospike is shown in Fig 4. An enlarged view of computational grid over the conical spike of different semi-cone angle  $\delta = 10^\circ$  to  $30^\circ$  is depicted in Fig. 5. The structured grid generation and the mono block is suitable to accommodate spike shape. As seen in the figures, these types of grids use quadrilateral cells in 2-dimensional in the computational array. The quadrilateral cells, which are very efficient at filling space, support a high amount of skew and stretching before the solution will be significantly affected. Additionally, the grid can be aligned with the flow, thereby yielding greater accuracy within the solver.

**RESULTS AND DISCUSSION**

The numerical procedure described in the previous section is here applied to compute flow field over the forward-facing spike attached to blunt body for Mach 6.0. Characteristic features of the flow field around the conical, hemispherical and flat-disc aero-spike attached to blunt body at high speeds are investigated with the help of velocity vector, density, pressure and Mach contours plots.

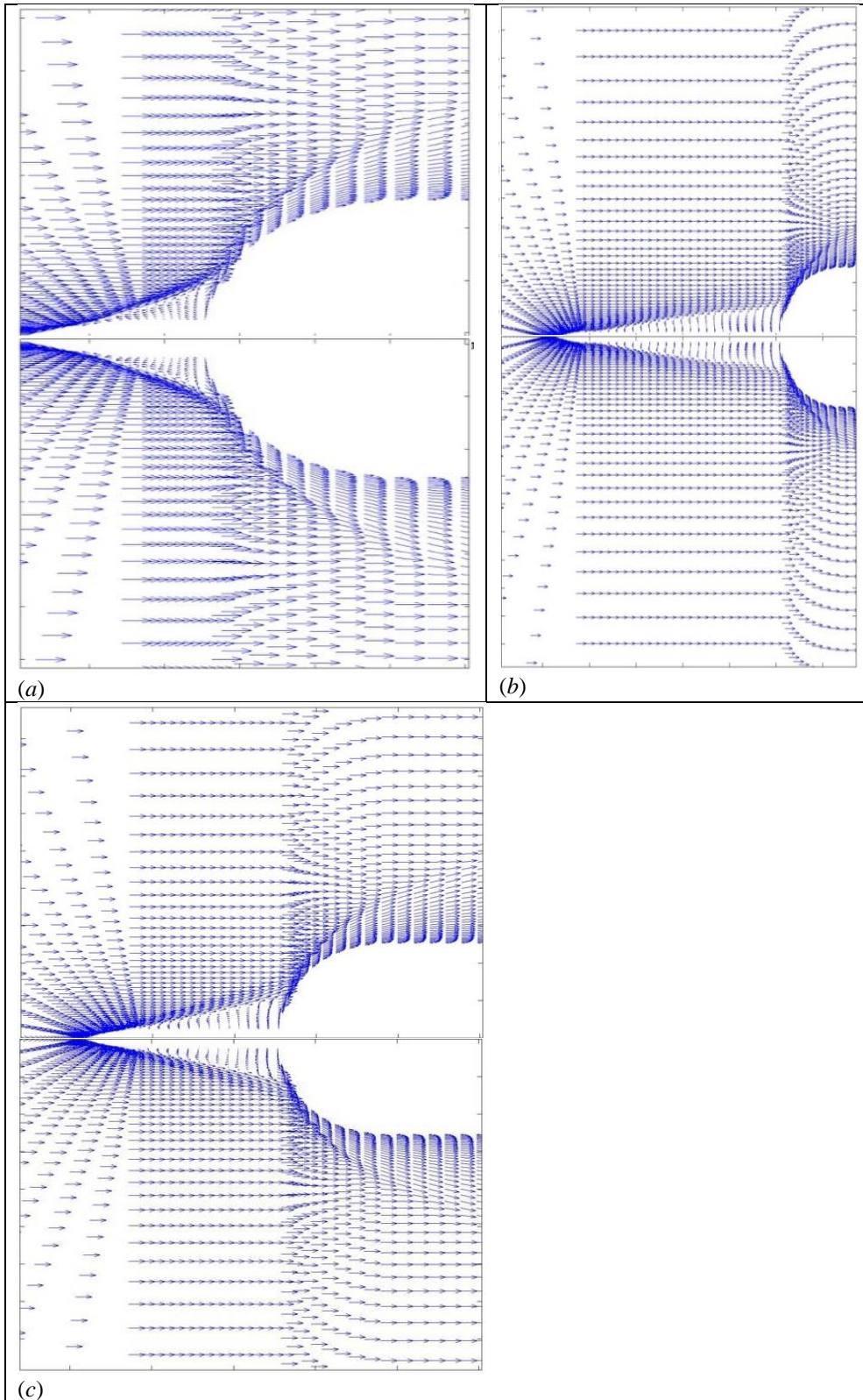


**Fig 6: Enlarged view of vector plot over a conical spike at semi-cone angle  $\delta = 10^\circ$  (a)  $L/D = 0.5$ , (b)  $L/D = 1.5$  and (c)  $L/D = 2.0$  attached to the hemispherical blunt body**

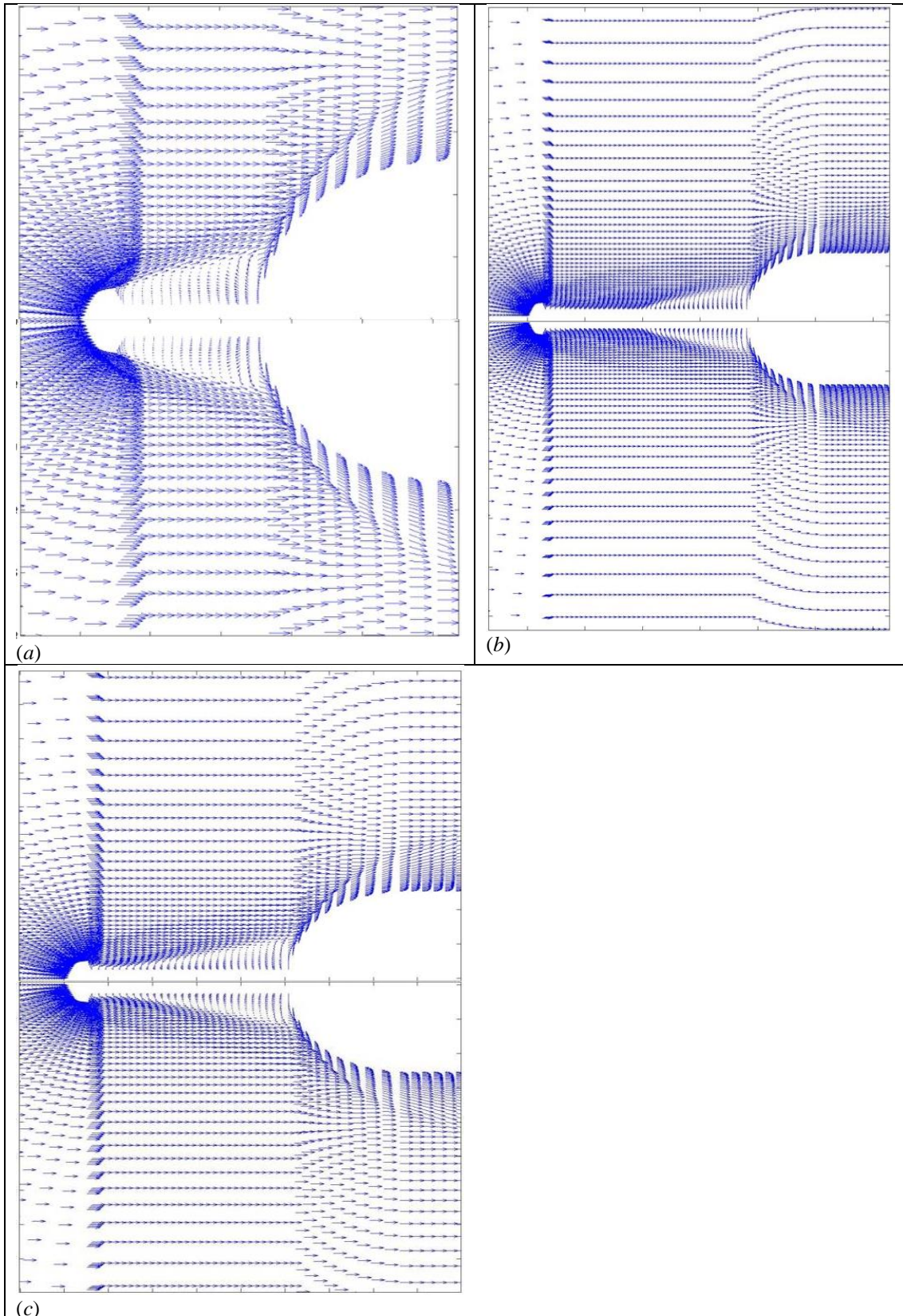


**Fig 7: Enlarged view of vector plot over a hemispherical disk spike at a  $L/D = 0.5, 1.5$  and  $2.0$  attached to the hemispherical blunt body**

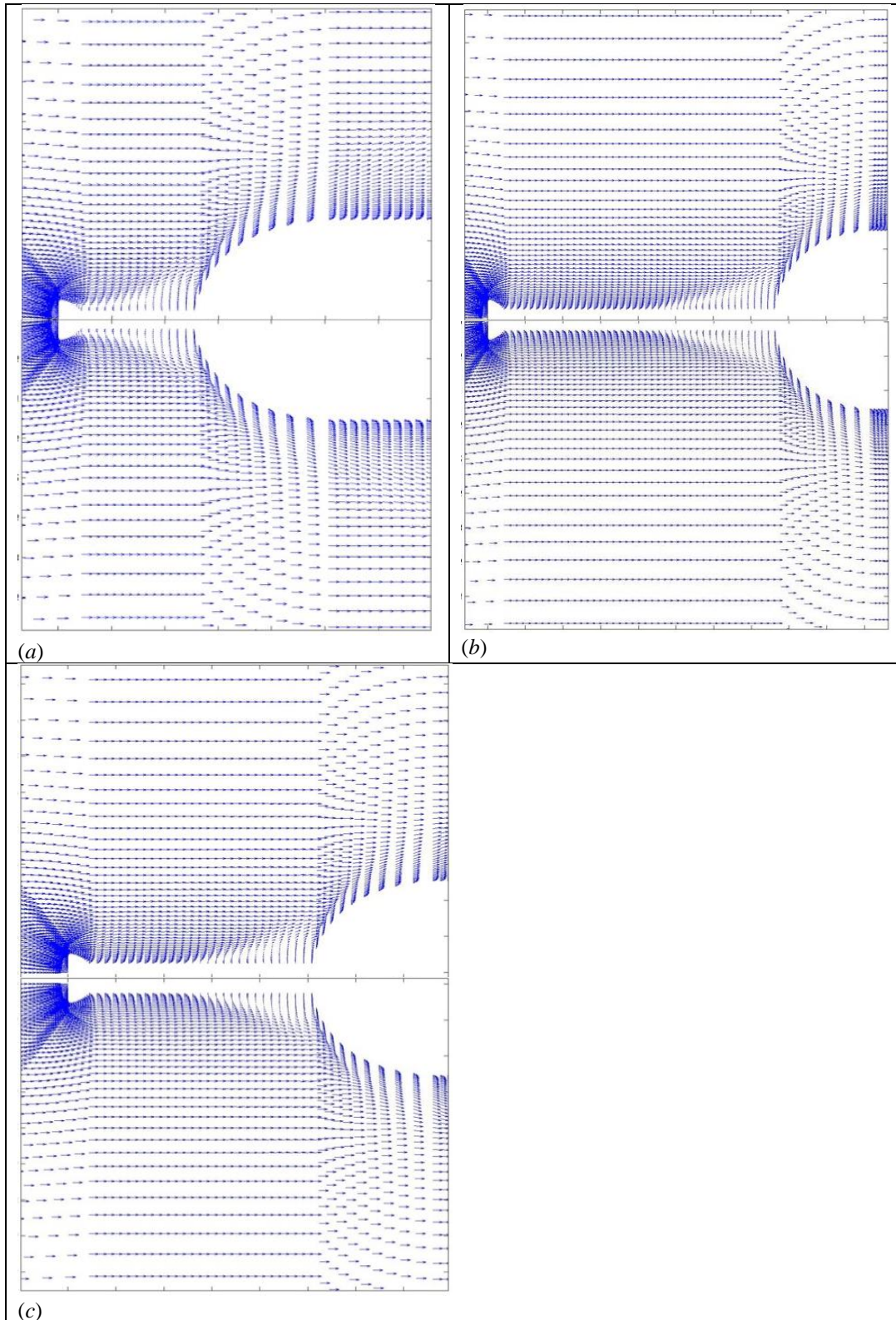


**Fig 8: Enlarged view of vector plot over a flat-faced disk spike at (a)  $L/D = 0.5$ , (b)  $L/D = 1.5$  and (c)  $L/D = 2.0$  attached to the hemispherical blunt body**

#### 4.1 Flow Characteristics

Figures 6 - 8 depict the velocity vector plots over the conical spike, the hemispherical aerospike, and the flat-disk aerospike for  $L/D = 0.5, 1.0,$  and  $2.0$  at Mach 6. It can be visualized from the vector plots that all the

significant flow field features such as conical shock wave, shear layer, reattachment shock and formation of the bow shock wave over the blunt body. Characteristic features of the flow field around the hemispherical body at Mach 6, such as bow shock wave ahead of the forward-

facing spike attached to the hemispherical and flat-disk aerospike are investigated with the help of velocity vector. The bow shock wave follows the aerospike contour and the fore-body is entirely subsonic up to the corner tangency point of the flat-faced and hemispherical aerospike where the sonic line is located. The effects of the sonic line on the aerodynamic design parameters have been investigated using the vector plots. A low pressure is formed immediately downstream of the base of spike hemispherical disc which is characterized by a low-speed recirculating flow region which can be attributed to the filling up of the growing space between the shock wave and the body.

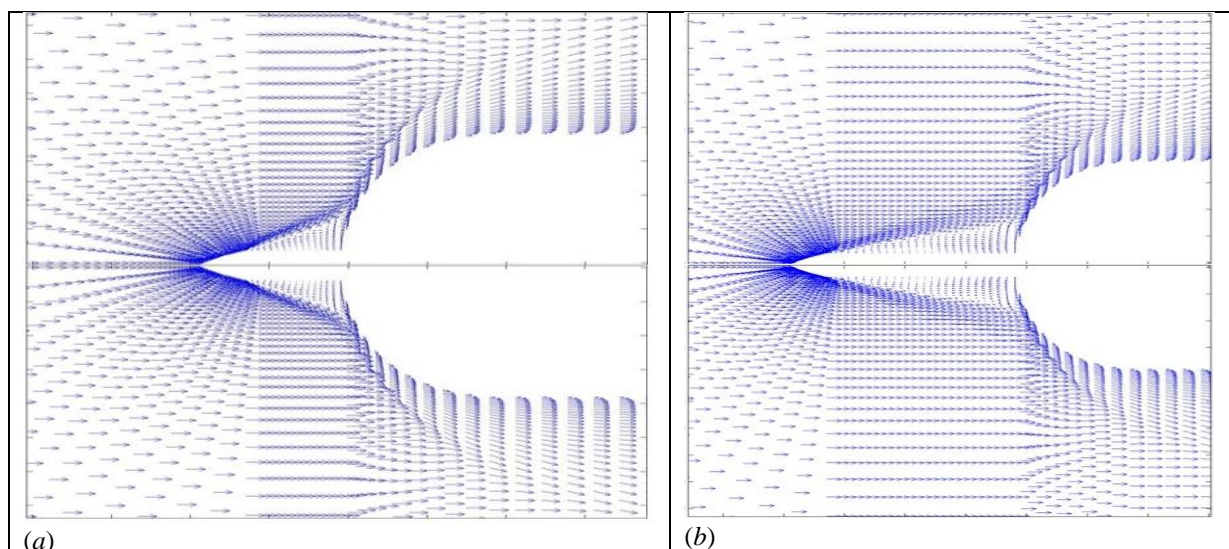
In Fig 6, interaction between the conical oblique shock wave starting from the tip of the spike and the reattachment shock wave of the blunt body can be visualized. The reflected reattachment wave and the shear layer from the interaction are seen behind the reattachment shock wave. A large separated region is observed in front of the blunt body and the shear layer; and the boundary of the separated region is clearly observed in Figs. 6 to 8. The separation zone depends on the shape of the spike and  $L/D$  ratio. Similar flow field features for the conical spike were observed by Yamauchi *et al.*, [13].

Figure 7 shows the velocity vector plots over the hemispherical aerospike for  $L/D = 0.5, 1.0$  and  $2.0$  at  $M_\infty = 6$ . The spiked body is completely enveloped within the recirculation region. Interaction between the conical oblique shock wave starting from the tip of the spike and the reattachment shock wave of the blunt body can be visualized in Fig. 7. The reflected reattachment wave and the shear layer from the interaction are seen behind the reattachment shock wave. A large separated region is observed in front of the hemispherical body and the shear layer; and the boundary of the separated region is clearly observed in the vector plots. Similar flow field features for the conical spike were observed by Yamauchi *et al.*,

[13]. The bow shock wave interacts with the reattachment shock generated by the blunt body. The interaction of the shock wave produced by the hemispherical aerospike differs significantly with the conical spike. The flow separation on the spike and recirculation zone formed on the blunt body cap depends on shape of the spike. The contour plots explain the cause of the drag reduction due to increase of the separation region over the spike.

Figure 8 displays the zoomed region of the vector plot on the flat-disk aerospike configurations. The bow shock wave follows the aerospike contour and the fore body is entirely subsonic up to the corner tangency point of the flat-faced and hemispherical aerospike where the sonic line is located. The effects of the subsonic flow on the hemispherical and flat disk bodies have been investigated by Truitt [23].

Figure 9 shows enlarged view of vector plot over a conical spike at conical spike at various value of  $\delta = 20^\circ, 25^\circ$  and  $30^\circ$  for  $L/D = 0.5, 1.5, 2.5$ . The effects of semi-cone angle are seen in the formation of conical oblique shock. The oblique shock angle and the reattachment shock on the hemispherical body depends on the semi-cone angle of the spike. The flow recirculation region with free shear layer and formation of the vortex flow in over the spike is captured well in the velocity vector plots. The variation of the semi-cone angle of  $10^\circ, 15^\circ, 20^\circ$  and  $30^\circ$  over the field does not show significant variation. The interaction between the conical oblique shock wave starting from the tip of the spike and the reattachment shock wave of the blunt body remains almost unchanged though the value of the  $\delta$  has been different. A large separated region is found in front of the blunt body and the shear layer; the boundary of the separated region is clearly visible in Fig 9.



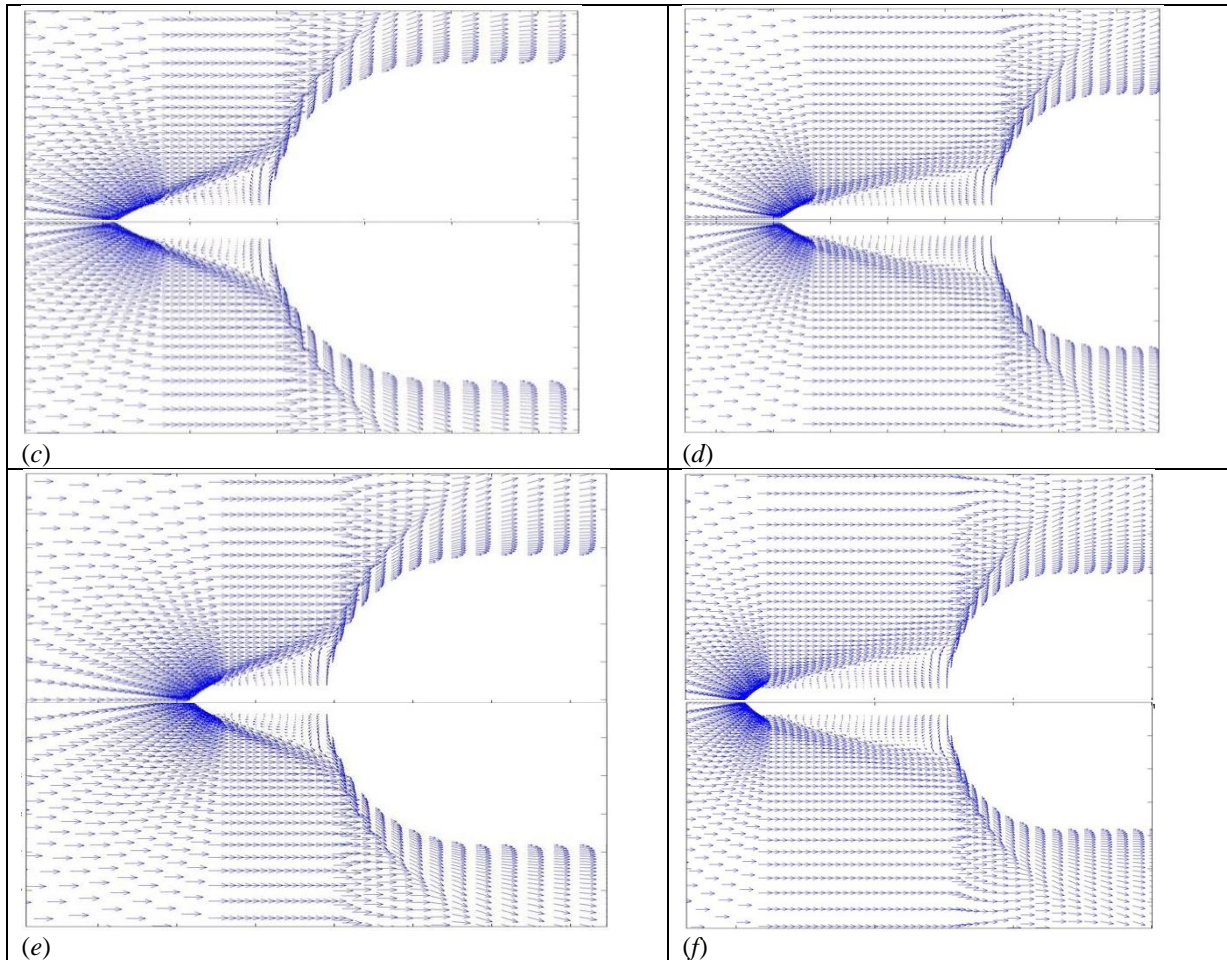


**Fig 9: Enlarged view of vector plot over a conical spike at (a)  $\delta = 15^\circ$ ,  $L/D = 1.5$  (b)  $\delta = 15^\circ$ ,  $L/D = 2.0$  (c)  $\delta = 20^\circ$ ,  $L/D = 1.5$  (d)  $\delta = 20^\circ$ ,  $L/D = 2.0$  (e)  $\delta = 25^\circ$ ,  $L/D = 1.5$  (f)  $\delta = 25^\circ$ ,  $L/D = 2.0$  attached to the hemispherical blunt body**

Figures 10–13 show Mach contours of the flow field around the hemispherical body with attached conical aerospikes, the hemispherical aerodisc and the flat-faced aerodisc with  $L/D = 0.5$ , 1.0 and 2.0. The flow fields are having significant differences between the aerospikes of the hemispherical aerodisc, flat-faced aerodisc and the conical spike as seen in the contour plots.

Figure 10 shows close-up view of Mach contour over a conical spike at semi-cone angle  $\delta = 10^\circ$  and  $L/D = 0.5$ ,  $L/D = 1.5$  and  $L/D = 2.0$  attached to the hemispherical body. The conical shock wave is emanated from the spike nose. The separated shear layer and the recompression shock from the reattachment point on the shoulder of the hemispherical body are visible. Flow patterns for  $L/D = 1.0$  and 2.0 are identical to that of  $L/D = 0.5$ . However, when the spike length is large, the angle of the oblique shock wave from the spike tip decreases, and the flow separation occurs slightly downstream. Because the reattachment point moves aft and the spike is relatively long, the length of the separated region extends. The angle of the conical shock wave depends on the angle of the shear layer, which gives an effective body shape to the outer freestream. Figure 10 shows the effects of the  $L/D$  ratio on the flow field. The conical

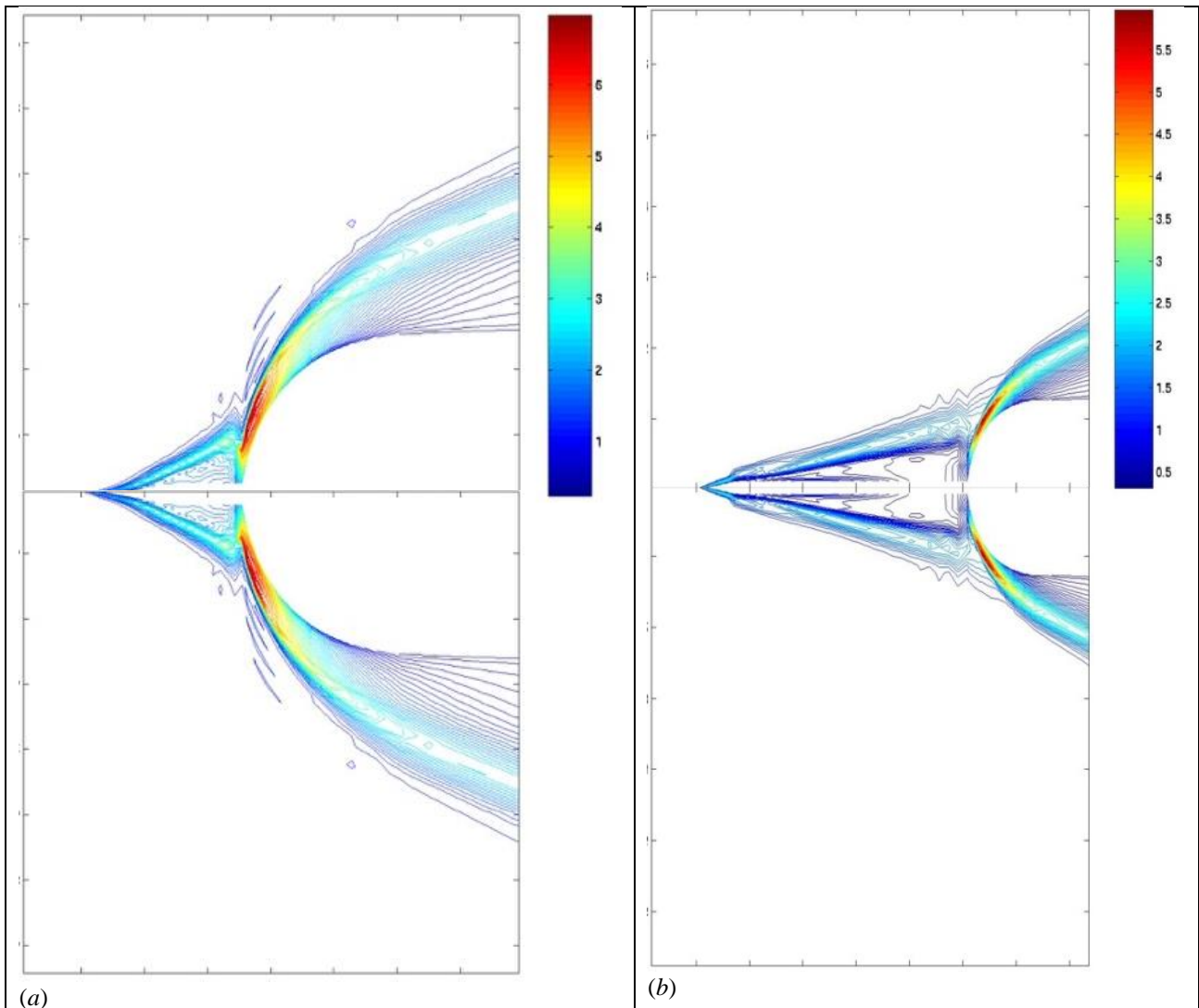
shock wave moves further away from the blunted body as compared to  $L/D = 0.5$  and 2.0 and the increase of  $L/D$  ratio increases the recirculation zone.

Figure 11 shows close-up view of Mach contours over a hemispherical disk spike at  $L/D = 0.5$ ,  $L/D = 1.5$  and  $L/D = 2.0$  attached to the hemispherical blunt body. Figure 12 shows close-up view of vector plot over a flat-faced disk spike at  $L/D = 0.5$ ,  $L/D = 1.5$  and  $L/D = 2.0$  attached to the hemispherical blunt body. In Fig 7(a), and (b), the interaction between the bow shock wave starting from the aero-disc of the spike and the reattachment shock wave of the blunt body is observed. The reflected reattachment wave and shear layer from the interaction are shown behind the reattachment shock wave. A large separated region is observed in front of the blunt body and the shear layer; the boundary of the separated region is clearly seen in Figs 11 and 12. In the aerodisk case as depicted in Figs. 11 and 12, the bow shock wave is emanating far from the hemispherical body. The bow shock wave generated from the aerodisk is affected by the  $L/D$  ratio. The body is completely enveloped within the recirculation region, which is separated from the inviscid flow within the bow shock wave by a separation shock. The bow shock interacts with the reattachment shock generated by the blunt body.

The interaction of the shock wave produced by the hemispherical aerospike differs significantly with the conical spike. The flow separation on the spike and recirculation zone formed on the blunt body cap depends on shape of the spike. The contour plots explain the cause of the drag reduction due to increase of the separation region over the aerodisk type of spike. The normal shock wave in front of the spike cap will reduce the drag as compared to without the spike. In the fore region of the aerodisk, the fluid decelerates through the bow shock wave. At the shoulder of the aerodisk or hemispherical cap, the flow turns and expands rapidly, the boundary layer detaches, forming a free shear layer that separates the inner recirculating flow region behind the base from

the outer flow field. The corner expansion over aerodisk process is a modified Prandtl-Mayer pattern distorted by the presence of the approaching boundary layer.

Figure 13 shows close-up view of Mach contours over a conical spike at  $\delta = 15^\circ, 20^\circ,$  and  $25^\circ, L/D = 1.5$  and  $2.0$  attached to the hemispherical blunt body. The conical shock angle can be calculated using the shock polar. In the downstream of the shock consists of recirculation area, which differs as compared to the formation of conical shock over the isolated cone. The shock wave in front of the spike cap will reduce the drag as compared to without the spike.



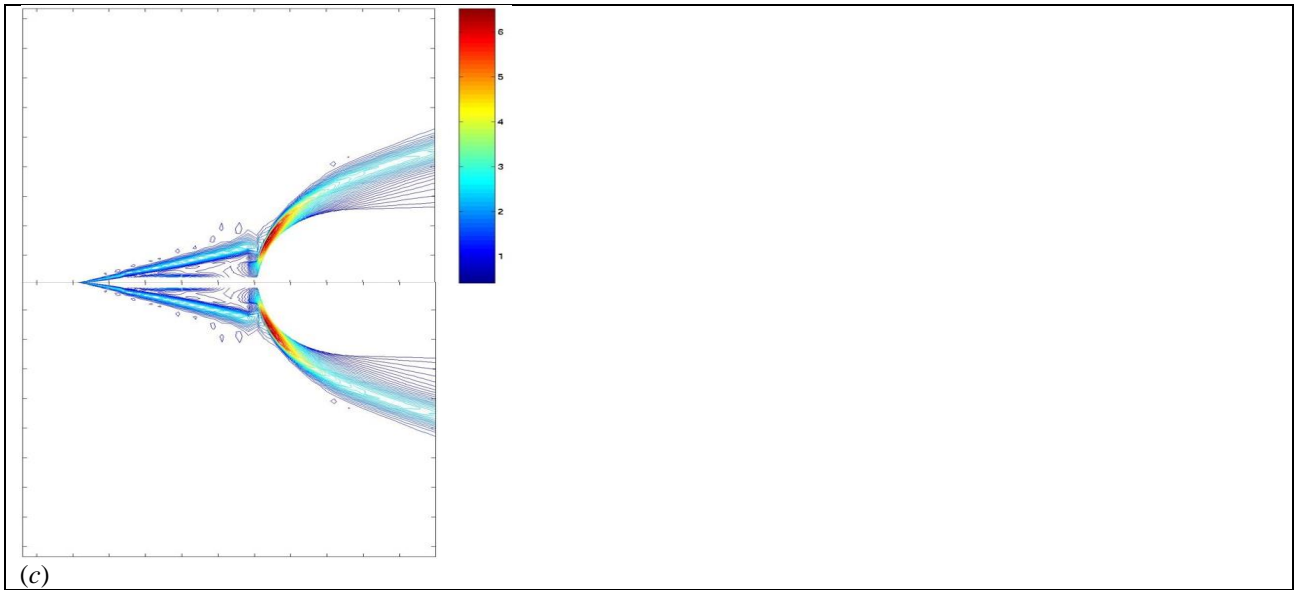


Fig 10: Close-up view of Mach contour over a conical spike at semi-cone angle  $\delta = 10^\circ$  (a)  $L/D = 0.5$ , (b)  $L/D = 1.5$  and (c)  $L/D = 2.0$  attached to the hemispherical blunt body

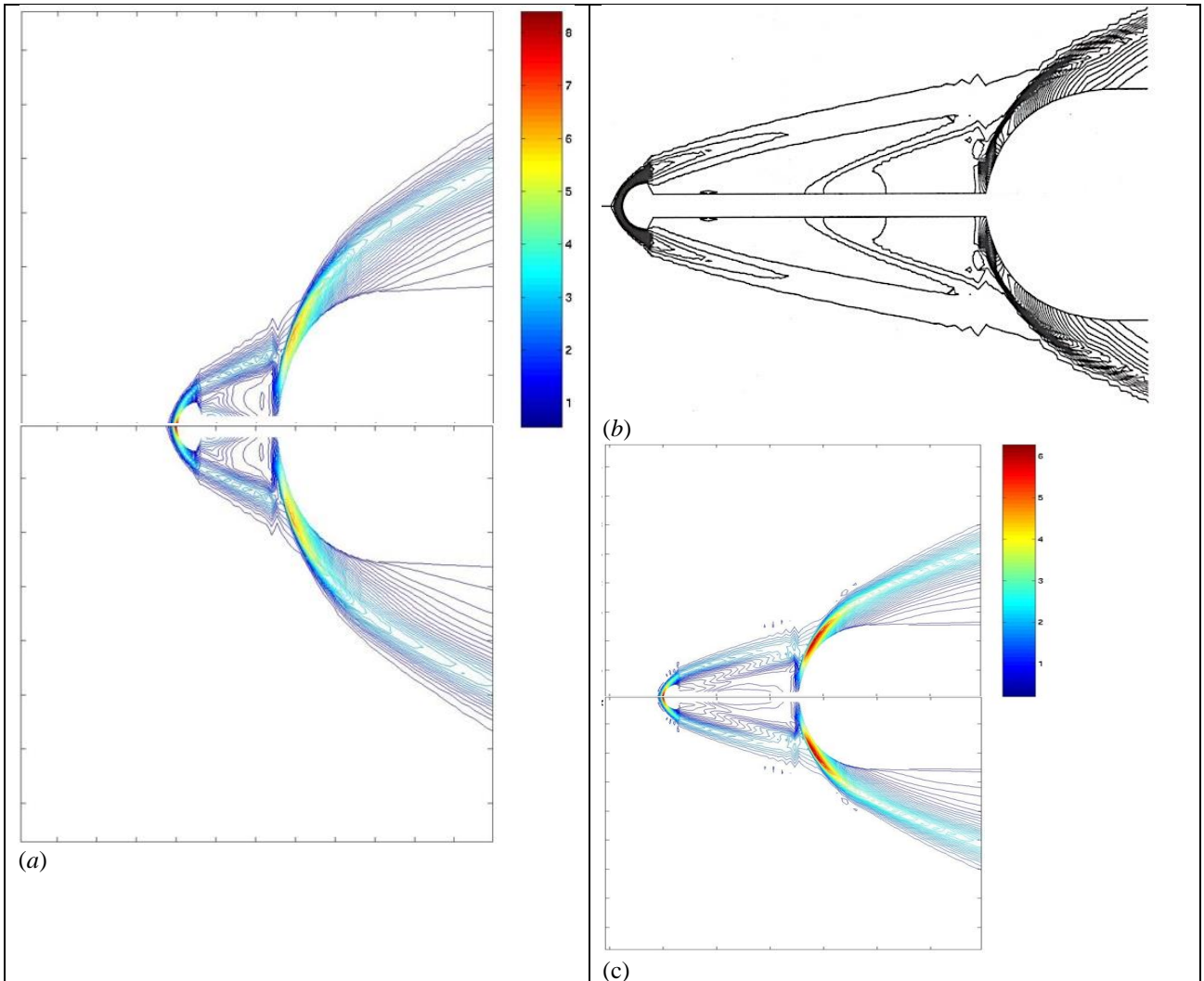
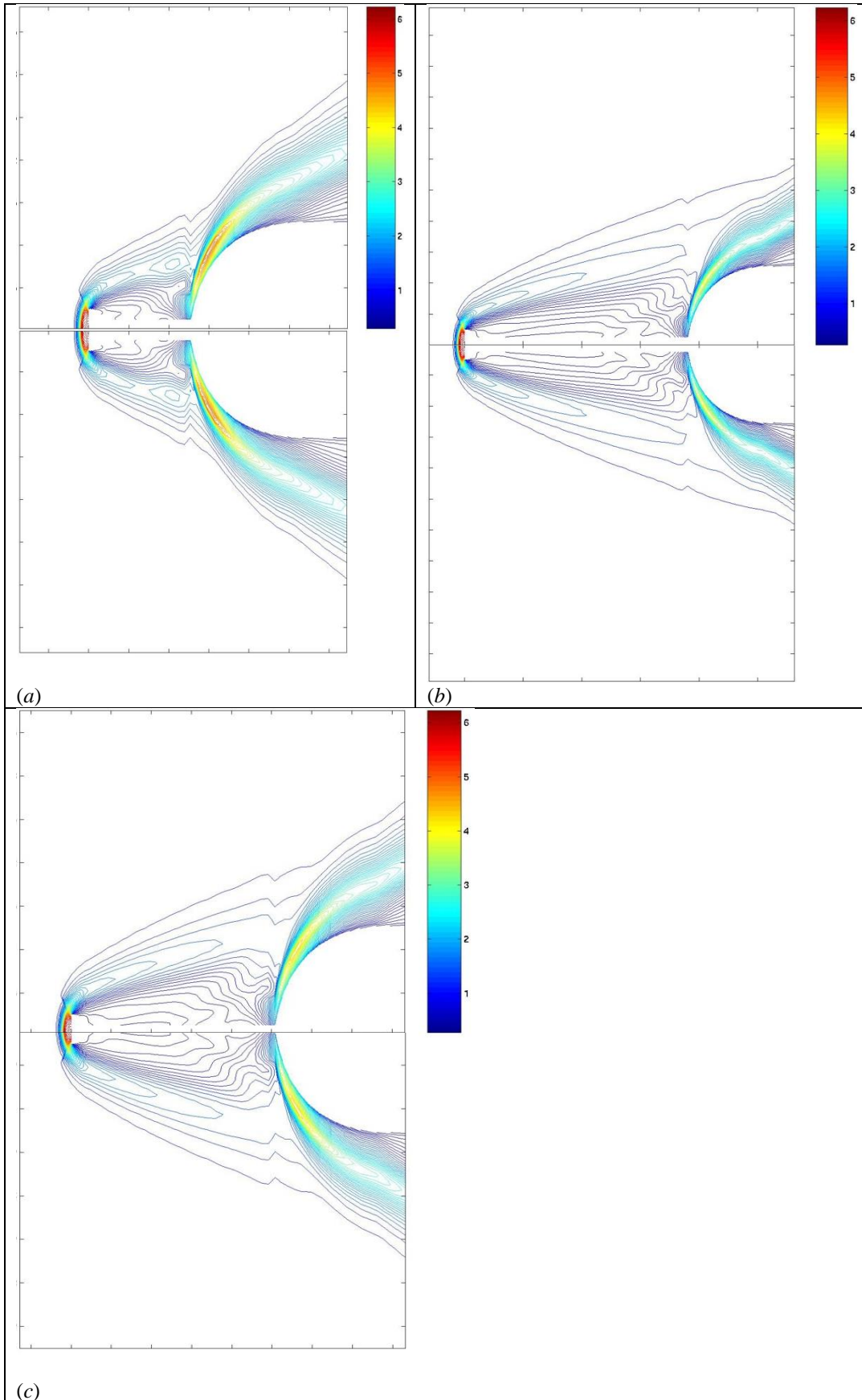


Fig 11: Close-up view of Mach contours over a hemispherical disk spike at (a)  $L/D = 0.5$ , (b)  $L/D = 1.5$  and (c)  $L/D = 2.0$  attached to the hemispherical blunt body



**Fig 12: Close-up view of vector plot over a flat-faced disk spike at (a)  $L/D = 0.5$ , (b)  $L/D = 1.5$  and (c)  $L/D = 2.0$  attached to the hemispherical blunt body**

## 4.2 Surface Pressure Distribution

Figures 14 – 16 show the pressure variation ( $p/p_a$ ) along the surface of the spiked hemispherical body for different semi-cone angle of the spike. The wall pressure  $p$  is normalized by free stream pressure  $p_a$ . The  $x/R = 0$  location is the spike/nose tip junction as shown in figure, where  $R$  is radius of the blunt body. Figures 14 -16 show the pressure variation along the spherical, the flat-disk and the conical spike, respectively, for the  $L/D = 0.5, 1.0$  and  $2.0$ . The pressure variation shows that the peak pressure falls as the  $L/D$  ratio increases. The relative behavior of the pressure distribution for  $L/D = 0.5, 1.0$  and  $2.0$  is shown in Figs 14 - 16. Pressure distribution shows the influence of the spike shape. It is interesting to note that the maximum pressure is found on the same location on the hemispherical body. A wavy pressure distribution is observed on the spike, which may be attributed to the numerical algorithm. The maximum as well as the global pressure level remain same. The location of the maximum pressure point remains same for all the cases. The maximum as well as the local pressure level decreases when  $L/D$  increases.

Figures 17 – 19 show the pressure distribution over the conical spike for various values of semi-cone angle  $10^\circ$  to  $30^\circ$ . It is important to mention here the effect of semi-cone angle and  $L/D$  ratio is not significant. The location of the maximum pressure on the surface of the spiked attached to hemisphere body is at a body angle of about  $40^\circ$  for all  $\delta$ . This location corresponds to the reattachment point.

## 4.3 Skin Friction Coefficient

Figures 20 - 22 show skin friction coefficient  $C_f$  variation over the conical spike, flat-face disc and hemispherical cap spikes for different  $L/D$  ratios and semi-cone angle of conical spike varied from  $10^\circ$  to  $30^\circ$ . The numerical simulation gives the effects of the subsonic region over the spike. The present work contains numerical studies for different spike geometries,  $L/D$  ratios and a semi-cone angle of  $10^\circ$  at Mach 6. Negative skin friction can be seen on the spike, which is due to the flow separation. The separation zone is found to be a function of the spike length as well as the shape of the spike. The region of the separation zone can be compared with the velocity vector plots as shown in Figs 6 - 10. A sharp and sudden rise of skin friction and heat flux is found very close to the conical spike tip, which is attributed to flow stagnation.

Figures 24 and 25 show the variation of skin friction coefficient  $C_f$  along the surface of the spike blunt body for various values of  $\delta$ . Negative skin friction can be seen on the spike, which is due to the ow separation. The separation zone is found to be a function of  $\delta$ . A sharp and sudden rise of skin friction is found very close to the spike tip, which is due to the flow stagnation. The secondary peak is observed at about the reattachment point.

## Oblique shock wave

Directly in front of the body an essentially normal shock is formed which extends around body as a oblique shock. A sufficient distance away from the body, the aerodynamic field is unaffected by the presence of the body. The strength of the shock decays continuously from its maximum value at the normal shock to a minimum strength or a Mach wave at infinity.

Although this diagram can be used for quantitative analysis and occasionally has been so employed, it primarily serves to complement perfect gas flow tables by providing a graphical display of the velocity vectors and wave geometry for all of the possible oblique shock wave solutions pertaining to a given freestream condition.

For high-speed flow past a cone at zero angle of attack, the shock wave angle  $\theta$  depends on the  $M_\infty$  and the cone angle  $\delta$ . The numerical analysis shows the shock wave angle is about  $14^\circ$ . The hodograph method is a powerful mathematical approach of two-dimensional flows which are either subsonic or mixed subsonic-supersonic [24, 25]. The change in variables is linear, thus allowing complex solutions to be formed by linear superposition of elementary solutions. Flow quantities on a circular cone with attached shock wave are constant on all concentric conical surfaces laying between the shock wave and the body, and so depend upon only one space variable. For high-speed flow past a cone at zero angle of attack, the shock wave angle  $\delta$  depends on the upstream Mach and the semi-cone angle  $\delta$ . The shock wave angle, the pressure coefficient, and the Mach number of the inviscid flow at the surface of the cone are given in Ref. [26] as a function of semi-cone angle  $\delta$  and oblique shock wave angle  $\theta$ . Fig. 1(a) has shown schematic sketch of supersonic flow over a cone. An approximate solution for axially symmetric ow over cone with attached shock is presented by Hord [27]. Zumwalt and Tang [28] have developed the approximate expression: relating the shock wave angle  $\theta$  to incoming Mach number  $M$  and the semi-cone angle  $\delta$ , for the axially symmetric flow past a cone with an attached shock wave.

Flow quantities on a circular cone with attached shock wave are constant on all concentric conical surface laying between the shock wave and the body, and so depend upon only one space variable. For high-speed flow past a cone at zero angle of attack, the shock wave (half) angle  $\theta$  depends on the upstream Mach and the semi-cone angle  $\delta$ . The shock wave angle, the pressure coefficient, and the Mach number of the inviscid flow at the surface of the cone are given in Ref. [26] as a function of  $\theta$  and  $\delta$ . Fig 1(d) shows schematic sketch of supersonic flow over a cone.

$$\frac{\tan(\delta-\theta)}{\tan \delta} = \frac{(\gamma-1)M_1^2 \sin^2 \delta + 1}{(\gamma+1)M_1^2 \sin^2 \delta} \dots\dots\dots (14)$$

Table 1 shows the variation of the semi-cone angle of cone with the conical shock wave angle. The conical shock wave angles are estimated using the velocity vector plots. It is difficult to calculate very accurately due to formation of shear layer and separated flow region over the spiked blunt body.

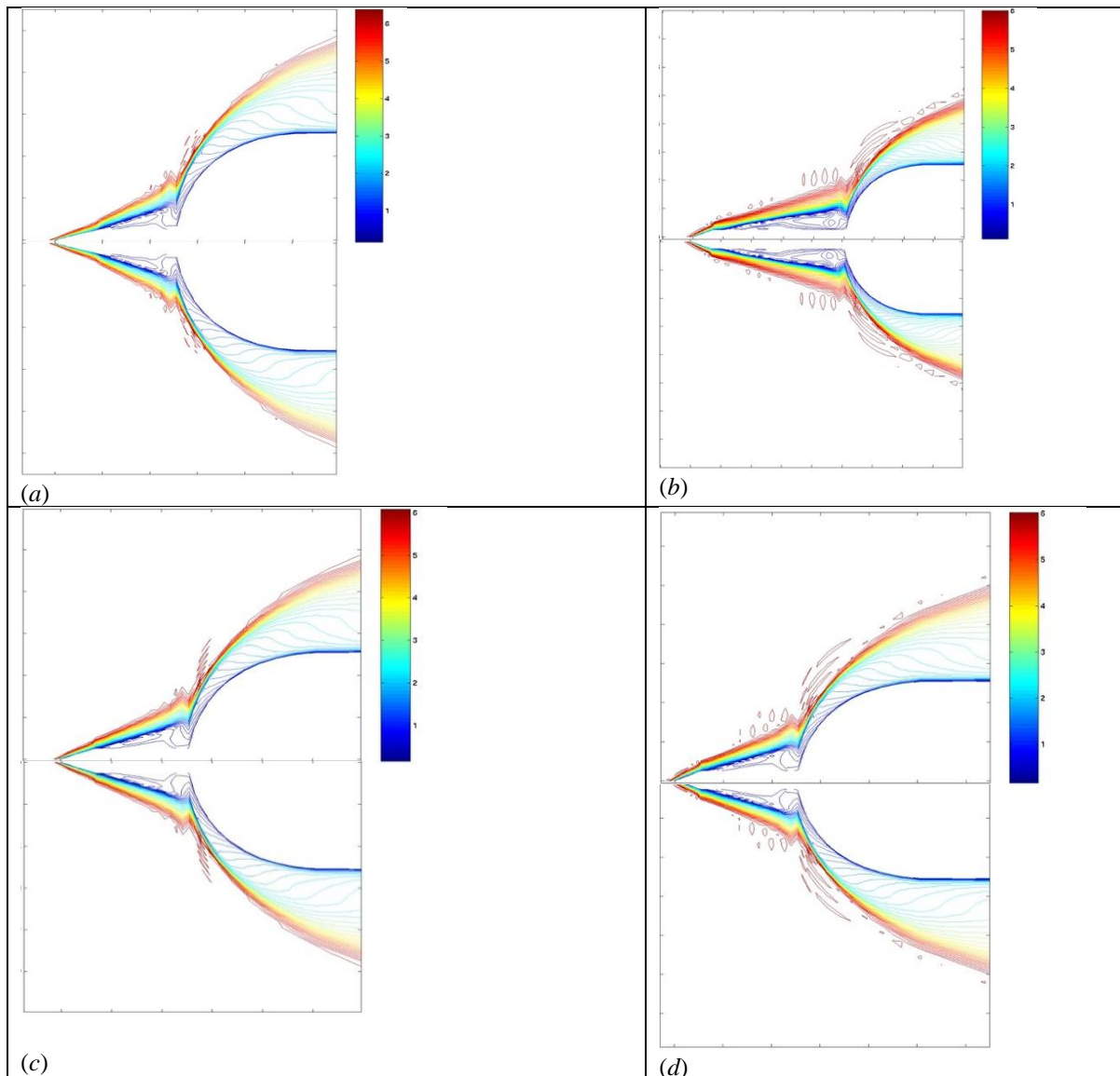
**Table 1: Conical shock wave angle**

Semi-cone angle	Oblique shock wave angle
10°	14.5°
15°	19.0°
20°	24.0°
30°	35.0°

The hodograph method is a powerful mathematical approach of two-dimensional flows which are either subsonic or mixed subsonic-supersonic [23]. The change in variables is linear, thus allowing complex solutions to be formed by linear superposition of elementary solutions. The flows over the cone are

described in a coordinate system which is at rest with respect to the shock. The upstream conditions are known and the solutions at the downstream are required to know. Flows on the two sides of the surface of discontinuity (shock) are related by the conservation of mass, momentum, and energy on the surface. These conservation laws need the respective fluxes to be continuous.

The change in variables is linear, thus allowing complex solutions to be formed by linear superposition of elementary solutions. The flows over the cone are described in a coordinate system which is at rest with respect to the shock. The upstream conditions are known and the solutions at the downstream are required to know. Flows on the two sides of the surface of discontinuity (shock) are related by the conservation of mass, momentum, and energy on the surface. These conservation laws need the respective fluxes to be continuous.



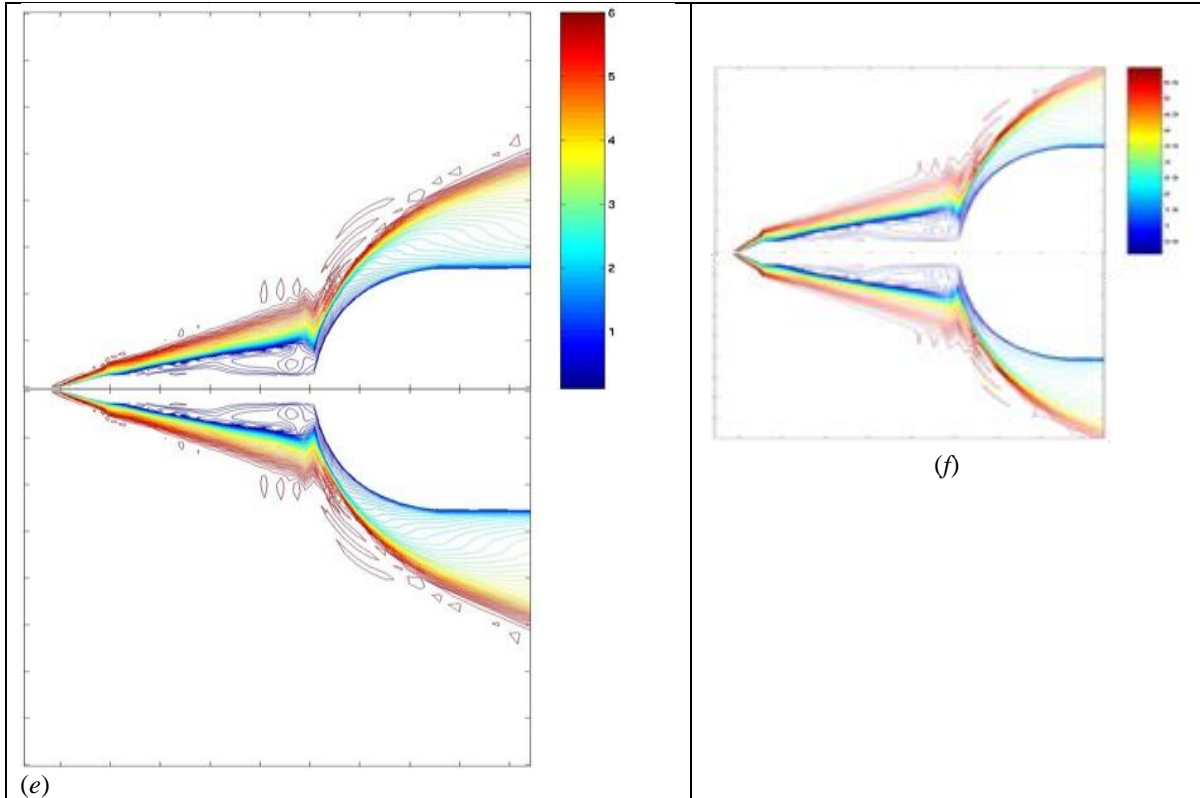


**Fig 13: Close-up view of Mach contours over a conical spike at (a)  $\delta = 15^\circ, L/D = 1.5$  (b)  $\delta = 15^\circ, L/D = 2.0$  (c)  $\delta = 20^\circ, L/D = 1.5$  (d)  $\delta = 20^\circ, L/D = 2.0$  (e)  $\delta = 25^\circ, L/D = 1.5$  (f)  $\delta = 25^\circ, L/D = 2.0$  attached to the hemispherical blunt body**

**Flow properties on stagnation point of hemispherical disc and flat-face disc**

Flow field at the stagnation point of the hemispherical disc and the flat-face disc as well as hemispherical body (without spike). The gas is assumed thermally perfect,  $p = \rho RT$  and calorically perfect  $h = c_p T$ . the ratio of the flow properties across the normal shock wave can be written as a function of freestream Mach number  $M_\infty$  and the ratio of specific heats  $\gamma$ , the relations are:

$$\frac{\rho_2}{\rho_\infty} = \frac{(\gamma+1)M_\infty^2}{(\gamma-1)M_\infty^2+2}$$

$$\frac{p_e}{p_\infty} = \frac{(\gamma+1)M_\infty^2}{(\gamma-1)M_\infty^2+2} \left[ 1 + \frac{\gamma-1}{2} \frac{(\gamma-1)M_\infty^2+2}{2\gamma M_\infty^2-\gamma+1} \right]^{1/(\gamma-1)} \dots\dots\dots (15)$$

$$\frac{p_e}{p_\infty} = \left[ \frac{(\gamma+1)M_\infty^2}{2} \right]^{\gamma/(\lambda-1)} \left[ \frac{\gamma+1}{2\gamma M_\infty^2+(\gamma-1)} \right]^{1/(\lambda-1)}$$

The freestream flow passes through the normal portion of the shock wave reaching state 2 and then decelerates isentropically to boundary layer edge  $e$  as shown in Fig 1(a) which constitutes the edge condition for the thermal boundary layer at the stagnation point.

If one assumes that the flow decelerates isentropically from the conditions at the stagnation point outside of the thermal boundary layer.

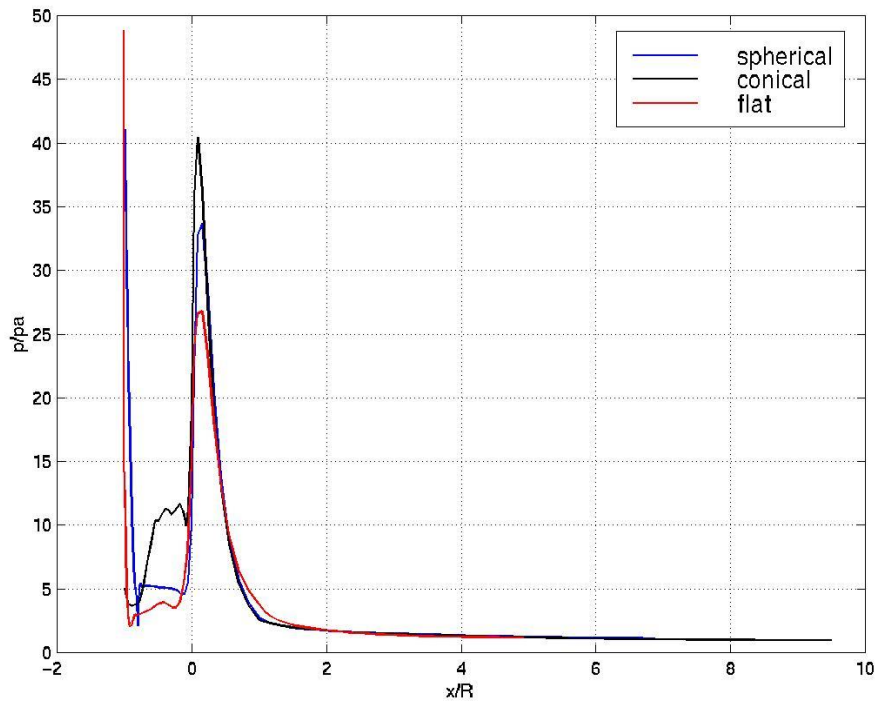


**Fig 14: Surface Pressure distribution over conical spike, flat-face disk spike and hemispherical disk spike attached to the hemispherical blunt body for  $L/D = 0.5$**

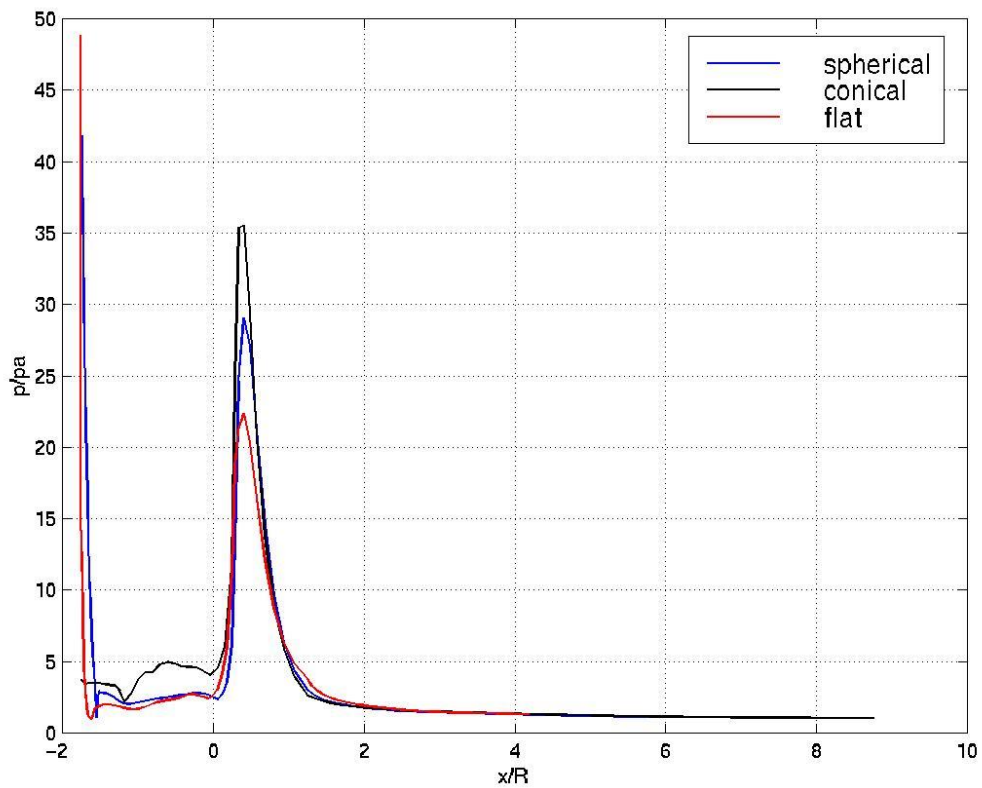


**Fig 15: Surface Pressure distribution over conical spike, flat-face disk spike and hemispherical disk spike attached to the hemispherical blunt body for  $L/D = 1.5$**

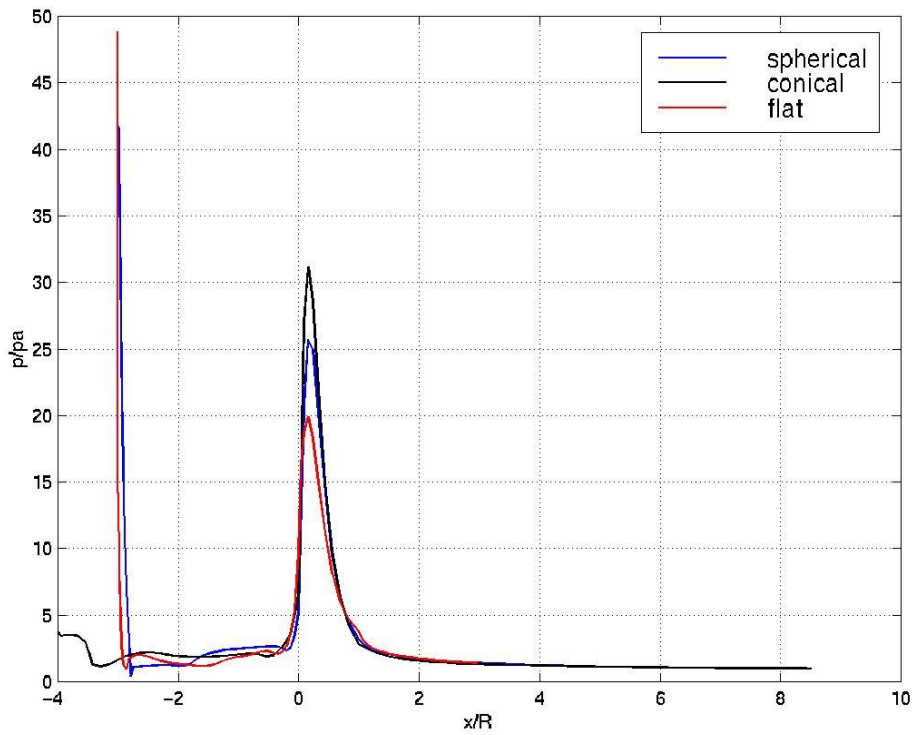


**Fig 16: Surface Pressure distribution over conical spike, flat-face disk spike and hemispherical disk spike attached to the hemispherical blunt body for  $L/D = 3.0$**

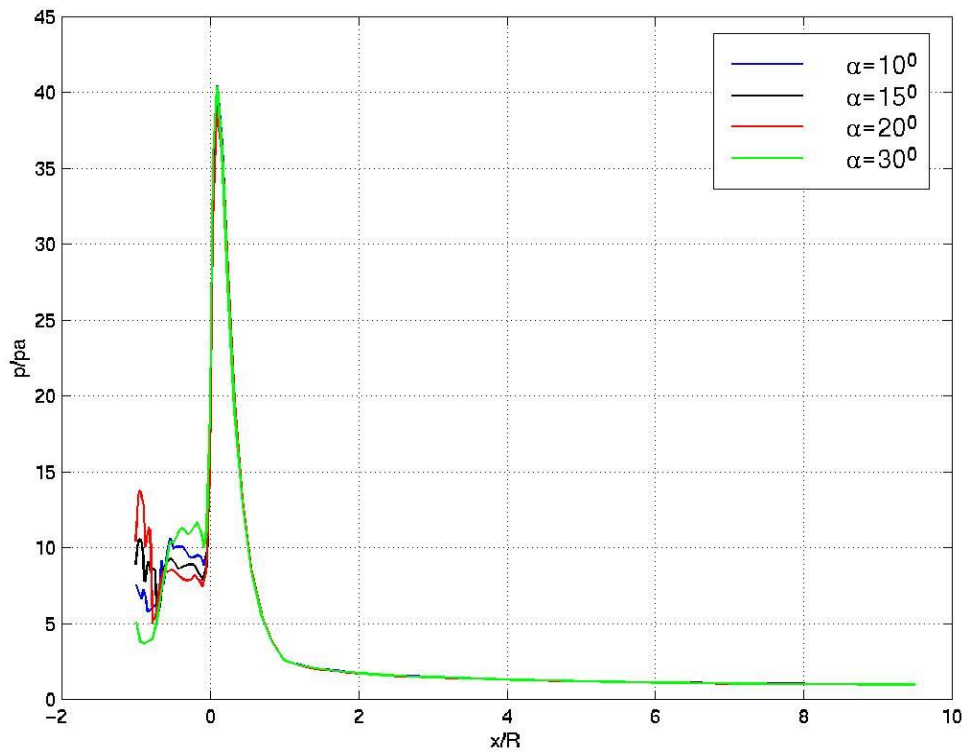


**Fig 17: Surface Pressure distribution over conical spike for different semi-cone angle attached to blunt body for  $L/D = 1.0$**

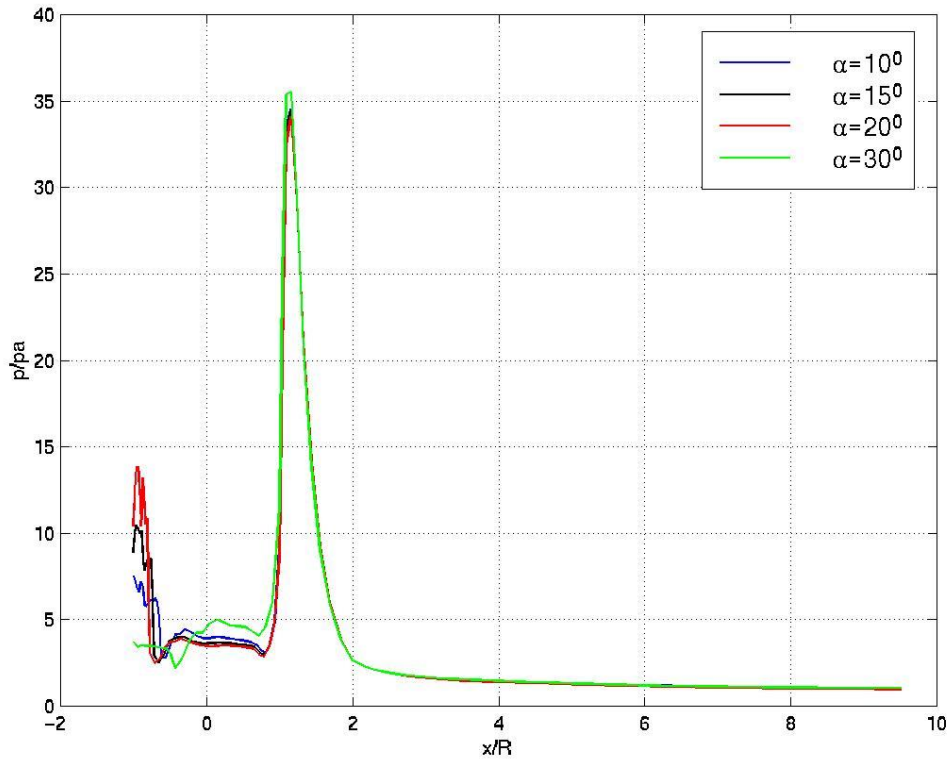


Fig 18: Surface Pressure distribution over conical spike for different semi-cone angle attached to blunt body for  $L/D = 1.5$

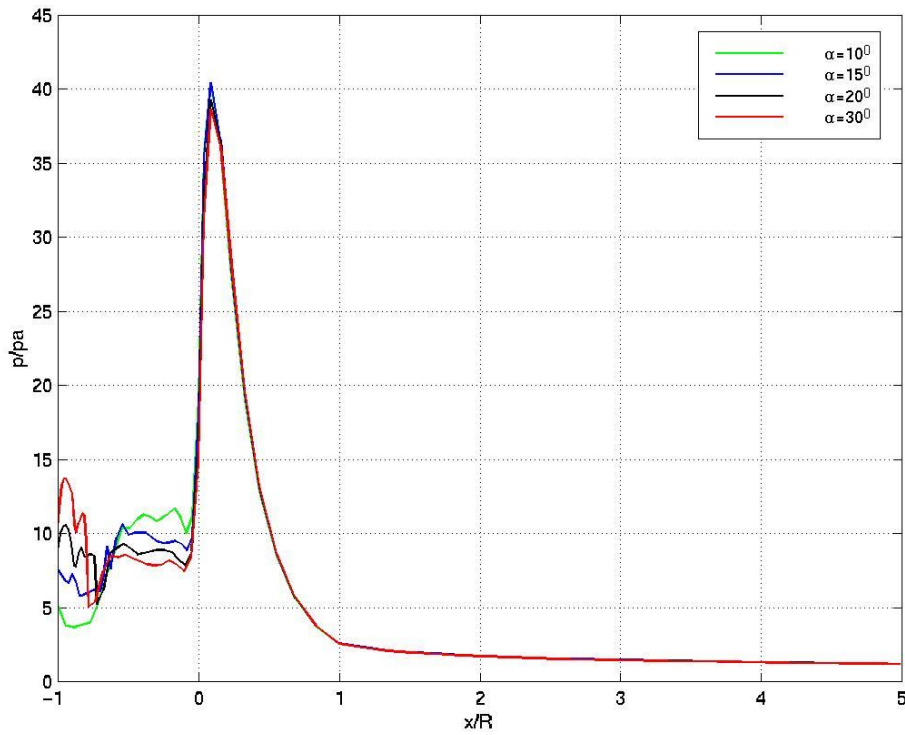
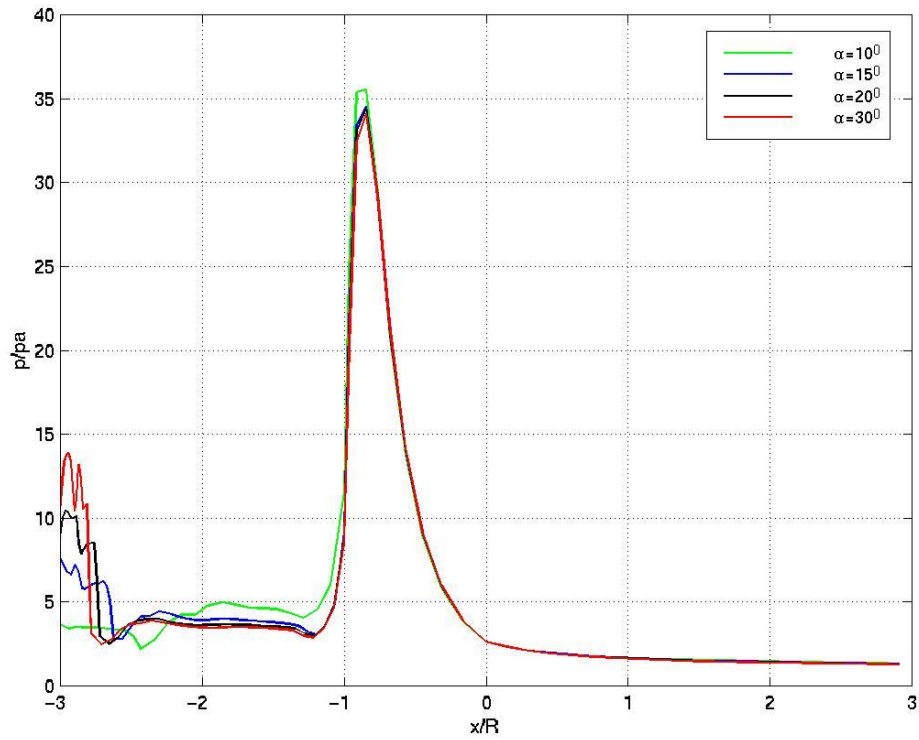
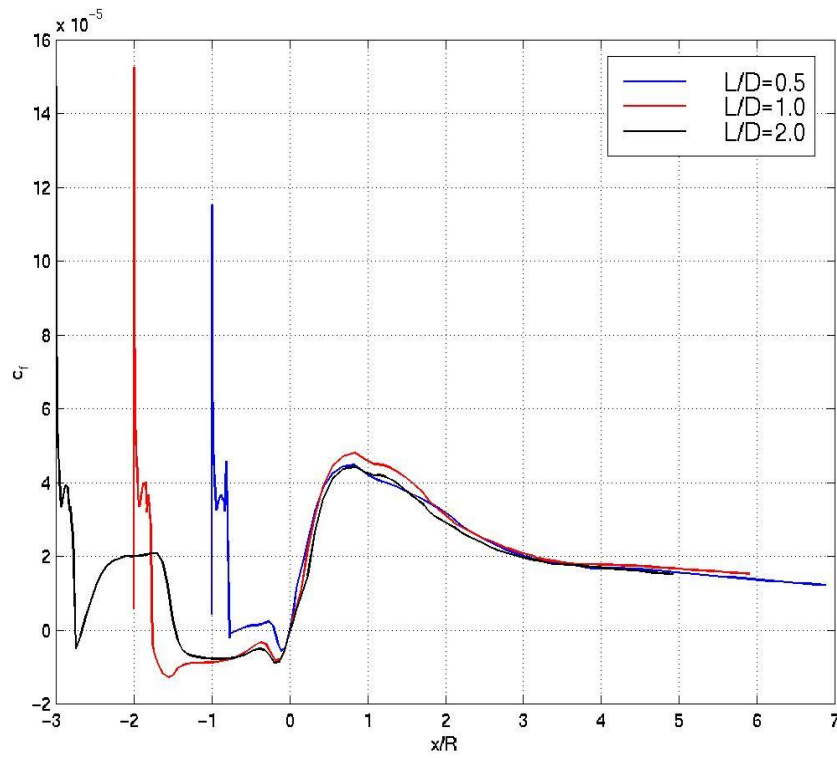


Fig 19: Surface Pressure distribution over conical spike for different semi-cone angle attached to blunt body for  $L/D = 1.0$



**Fig 20: Surface Pressure distribution over conical spike for different semi-cone angle attached to blunt body for  $L/D = 3.0$**



**Fig 21: Skin friction distribution over conical spike for semi-cone angle of  $10^\circ$  attached to a blunt body for  $L/D = 0.5, 1.0$  and  $2.0$**

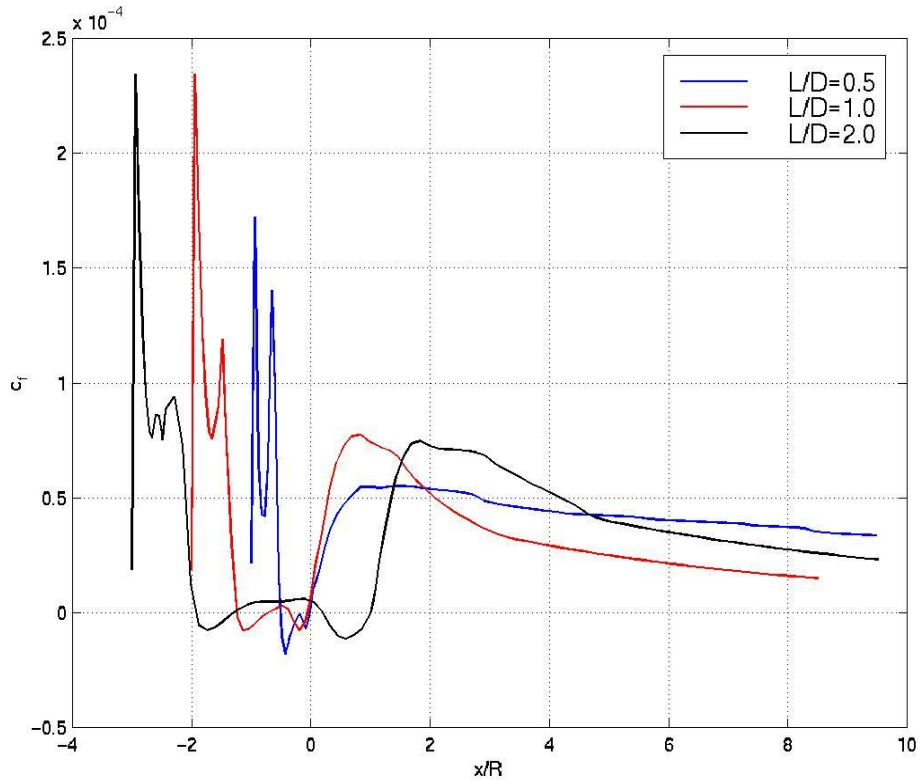


**Fig 22: Skin friction distribution over flat-face disk spike attached to a blunt body for  $L/D = 0.5, 1.0$  and  $2.0$**

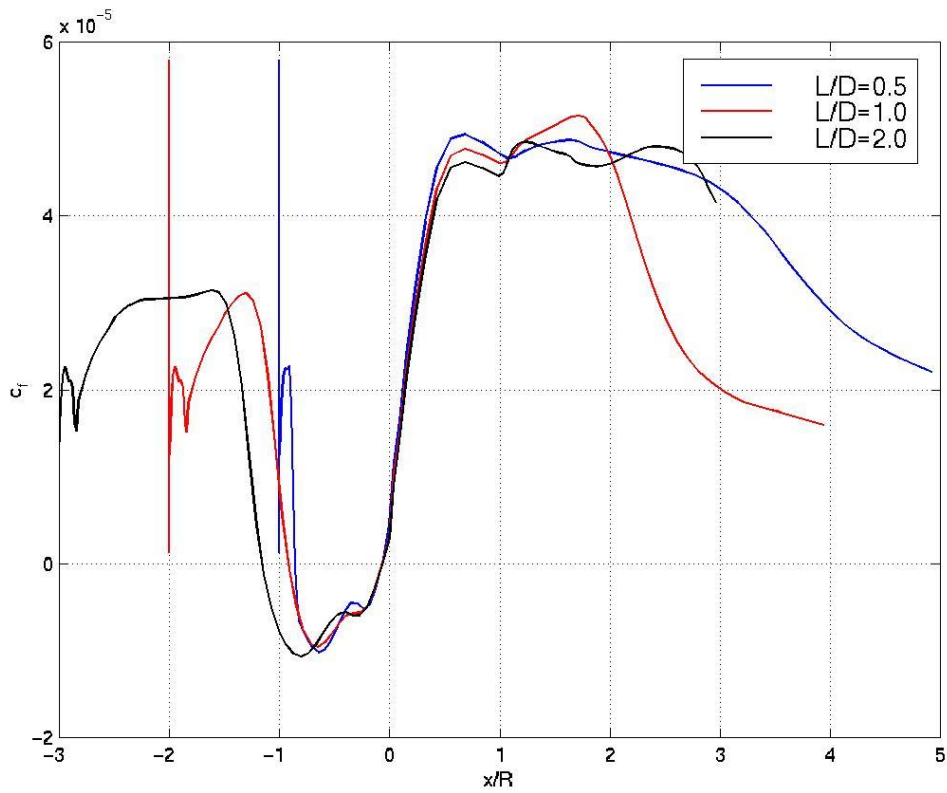


**Fig 23: Skin friction distribution over hemispherical disk spike attached to a hemispherical body for  $L/D = 0.5, 1.0$  and  $2.0$**

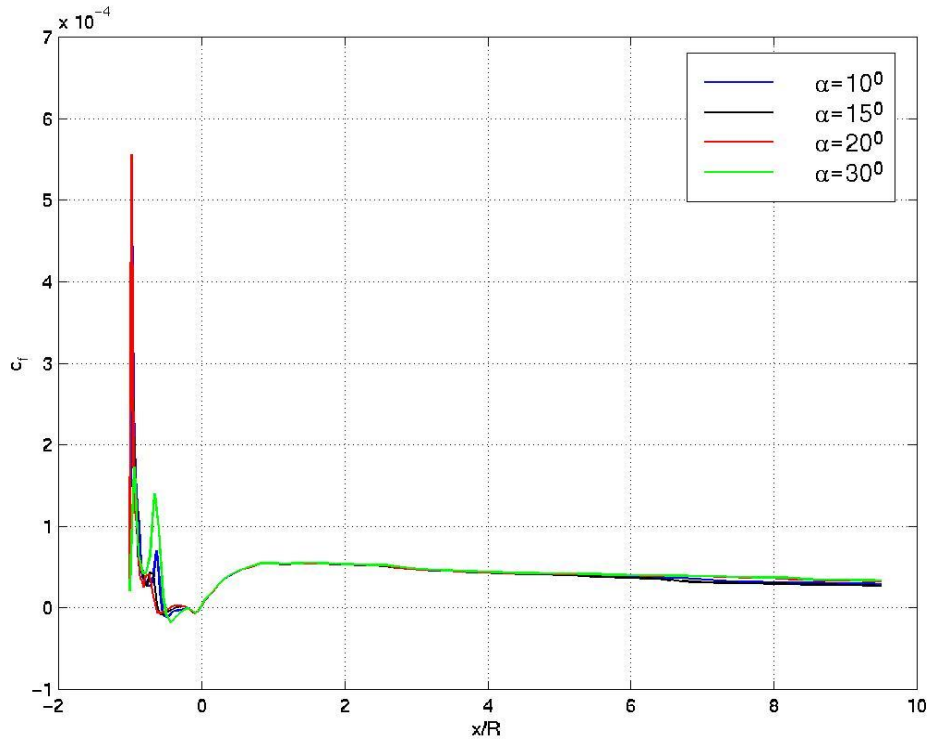


**Fig 24: Skin friction distribution over conical spike for different semi-cone angle attached to hemispherical body for  $L/D = 1.0$**

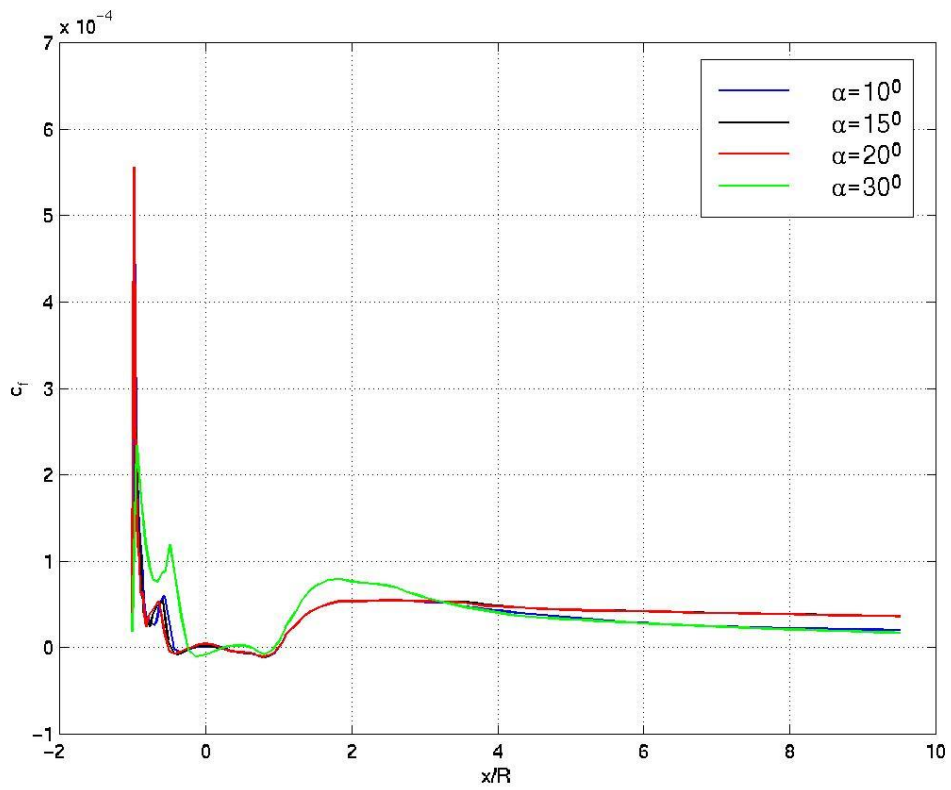


**Fig 25: Skin friction distribution over conical spike for different semi-cone angle attached to blunt body for  $L/D = 1.0$**

**Shock distance for hemispherical disc and flat-face disc**

Shock distance on the hemispherical shape spike and flat-face spike is shown in Fig. 1(e) and (f), respectively. The flow fields differ between the hemispherical shape spike and the flat-faced are illustrated in schematic sketch in Fig 1. In the flat-face region of the aerodisk, the fluid decelerates through the bow shock wave. At the shoulder of the aerodisk or hemispherical cap, the flow turns and expands rapidly, the boundary layer detaches, forming a free shear layer that separates the inner recirculating flow region behind the base from the outer flow field. The corner expansion over aerodisk process is a modified Prandtl-Mayer pattern distorted by the presence of the approaching boundary layer.

For the case of flat-nosed spike flying at hypersonic speeds, a detached bow wave is formed in front of the nose which is practically normal at the body axis. Since the flow behind the normal shock is always subsonic, simple continuity considerations show that the shock-detachment distance and stagnation-velocity gradient are essentially a function of the density ratio across the shock. The shock-detachment distance becomes smaller with increasing density ratio. For the case of flat-nosed spike flying at hypersonic speeds, a detached bow wave is formed in front of the nose which is practically normal at the body axis. Since the flow behind the normal shock is always subsonic, simple continuity considerations show that the shock-detachment distance and stagnation-velocity gradient are essentially a function of the density ratio across the shock. The shock-detachment distance becomes smaller with increasing density ratio. Probstein [29] gives expression for the shock detachment distance  $\Delta_F$  with diameter of the flat-disk  $D_S$  ratio as:

$$\frac{\Delta_F}{D_S} = 2.8 \sqrt{\frac{\rho_\infty}{\rho_0}} \dots\dots\dots (16)$$

Where the density ratio across the normal shock [24] is:

$$\epsilon = \frac{\rho_\infty}{\rho_0} = \frac{(\gamma-1)M_\infty^2 + 2}{(\gamma+1)M_\infty^2} \dots\dots\dots (17)$$

The ratio of shock stand-off distance  $\Delta_S$  with hemispherical spike of diameter,  $D_S$  is:

$$\frac{\Delta_S}{D_S} = \frac{2\epsilon}{1 + \sqrt{\frac{8\epsilon}{3}}} \dots\dots\dots (18)$$

The values of  $\Delta_F$  and  $\Delta_S$  are found 0.1898 and 0.1109, respectively. The numerical values of the ratio of shock stand-off to spike cap diameter are calculated from the velocity vector and pressure contour plot and they are 0.19 and 0.11 which show good agreement with the analytical values.

**Wave drag**

The contour plots reveal the flow field behavior over the spike and also the drag reduction mechanism due to interaction of the shock waves, which is influenced by the spike configurations as observed in the velocity vector plots. As the spike nose becomes large from a conical nose to a flat-faced nose, the wave drag decreases.

The effects of the geometrical parameters on the aerodynamic drag are investigated. The flow field was computed for Mach 6 and for  $L/D = 0.5, 1.0$  and  $2.0$ . The main purpose of the numerical simulation is to find out the effects of the subsonic region over the spike.

$$C_D = \frac{\int_S F_x dS}{\frac{1}{2} \rho_\infty V_\infty^2 S_0} \dots\dots\dots (19)$$

Where  $F_x$  is the axial pressure component,  $dS$  is the area of the segment and reference surface area is  $S_0 = 0.25\pi D^2$ . The aerodynamic drag is computed for different spike geometries,  $L/D$  ratio and semi-cone angle at Mach 6. As the curvature radius of the spike nose becomes large from a conical nose to a flat-faced nose, the wave drag decreases. From the flow field point of view, the aerodisk with  $L/D = 2.0$  has the potential for the greatest drag reduction in this computational result. It was found by them that the aerodisk spike has shown a better drag reduction capability in comparison to the other types of aerospike configurations. Table 1 gives the computed value of the drag coefficient for the three different spike configurations. The comparisons of the drag on each of the spiked blunt body. The contour plots reveal the flow field behavior over the spike and also the drag reduction mechanism due to interaction of the shock waves, which is influenced by the spike configurations as observed in the velocity vector plots. As the spike nose becomes large from a conical nose to a flat-faced nose, the wave drag decreases.

Table 2 shows the computed value of the drag coefficient for the three different spike configurations. The comparisons of the drag on each of the spiked blunt body configuration (conical, disk and flat-face) can be observed. The aerodynamic drag coefficient of hemisphere-cylinder without spike is 0.91. Therefore, it is worth to mention here that forward-facing spike attached to a hemisphere-cylinder is advantageous for drag reduction. Table 3 shows the aerodynamic drag for the conical spike for different semi-cone angle of cone. This is also noticed in the above flow field visualizations. The drag on a cone is smaller than that on a blunt body without the spike. As expected, the drag of the blunt body is There is marginal effect on the drag due to change of conical angle remarkably influenced by the spike length and spike shape. Thus, the drag is reduced because of the existence of the separated region created by the spike on the nose. With an increase in the length, the separated flow at the nose is extended.

**Table 2: Aerodynamic Drag over the spike**

Spike geometry	$L/D = 0.5$	$L/D = 1.0$	$L/D = 2.0$
Conical spike	0.868	0.582	0.384
Hemisphere disc	0.576	0.317	0.231
Flat Face disc	0.458	0.309	0.277

**Table 3: Aerodynamic Drag over the conical spike for different semi-cone angle**

	$\delta = 10^\circ$	$\delta = 15^\circ$	$\delta = 20^\circ$	$\delta = 25^\circ$
$L/D = 0.5$	.70762E+00	.71153E+00	.70196E+00	.69650E+00
$L/D = 1.5$	.67886E+00	—	—	—
$L/D = 2.0$	60743E+00	.65278E+00	65179E+00	.64744E+00

It is important to note that the spike is advantageous for drag reduction. This is also noticed in the above flow field visualizations. The drag on a cone is smaller than that on a blunt body without the spike. As expected, the drag of the blunt body is remarkably influenced by the spike length and spike shape. Thus, the drag is reduced because of the existence of the separated region created by the spike on the nose. With an increase in the length, the separated flow at the nose is extended.

## CONCLUSION

The flow field over a spiked blunt body of axisymmetric configuration is studied numerically by solving time-dependent compressible Navier-Stokes equations at Mach 6. The governing fluid flow equations are discretized in spatial coordinates employing a finite volume approach which reduces the equations to semi-discretized ordinary differential equations. Temporal integration is performed using the two-stage Runge-Kutta time stepping scheme. Flow field around the conical spiked blunt body have been calculated for different semi-cone angle of the spike. The essential flow field features around the spike are captured. The effects of different spike cone angle have been numerically investigated which will be useful for understanding flow field in conjunction with shock polar. The influence of the shape of the spike and length to diameter ratios, flow visualizations were performed using the velocity vector and contour plots. The reduction in the pressure ahead of the blunt body gives the drag reduction. The reattachment point can be moved backward or removed, which depends on the spike length or the nose configuration. However, because of the reattachment of the shear layer on the shoulder of the hemispherical body, the pressure near that point becomes large. The ratio of the spike length to spike diameter influences the aerodynamic drag reduction mechanism.

## REFERENCES

- Bogdonoff, S. M., & Vas, I. E. (1959). Preliminary Investigations of Spike Bodies at Hypersonic Speeds. *Jr. of the Aerospace Sciences*, 26(2), 65-74.
- Maull, D. J. (1960). Hypersonic Flow over Symmetric Spiked Bodies. *Journal of Fluid Mechanics*, 8, 584.
- Wood, C. J. (1961). Hypersonic Flow over Spiked Cones. *Journal of Fluid Mechanics*, 12, 614.
- Menezes, V., Saravanan, S., Jagdeesh, G., & Reddy, K. P. (2003). Experimental Investigation of Hypersonic Flow Over Highly Blunted Cones with Aerospikes. *AIAA Journal*, 41(10), 1955-1966.
- Kobayashi, H., Maru, Y., & Fukiba, K. (2007). Experimental Study on Aerodynamic Characteristics of Telescopic Aerospikes with Multiple Disks. *Journal of Spacecraft and Rockets*, 44(1), 33-41.
- Milicv, S. S., Pavlovic, M. D., Ristic, S., & Vitic, A. (2002). "On the Influence of Spike Shape at Supersonic Flow Past Blunt Bodies", Faculty Universities, Series: Mechanics, Automatic Control and Robotic, 3(12), 371-382.
- Caarese, W., & Hankey, W. L. (1985). Modes of Shock Wave Oscillations on Spike Tipped Bodies. *AIAA Journal*, 23(2), 185-192.
- Hahn, M. (1966). Pressure Distribution and Mass Injection Effects in the Transitional Separated Flow Over a Spiked Body at Supersonic Speed. *Journal of Fluid Mechanics*, 24(2), 209-223.
- Milicev, S. S., & Pavlovic, M. D. (2002). Influence of Spike Shape at Supersonic Flow Past Blunt Nosed Bodies Experimental Study. *AIAA Journal*, 40(5), 1018-1020.
- Kubota, H. (2004). Some Aerodynamic and Aerothermodynamic Considerations for Reusable Launch Vehicles, AIAA-2004-2428.
- Crawford, D. H. (1959). Investigation of the Flow over a Spiked-nose Hemisphere at a Mach number of 6.8, NASA TN-D 118.
- Motoyama, N., Mihara, K., Miyajima, R., Watanuki, W., & Kubota, H. (2001). Thermal Protection and Drag reduction with Use of Spike in Hypersonic Flow, AIAA Paper 2001-1828.
- Yamauchi, M., Fujjii, K., Tamura, Y., & Higashino, F. (1993). Numerical investigation of Hypersonic Flow Around a Spiked Blunt Body. AIAA paper 93-0887.

14. Shoemaker, J. M. (1990). Aerodynamic Spike Flowfields Computed to Select Optimum Configuration at Mach 2.5 with Experimental Validation. AIAA Paper 90-0414.
15. Fujita, M., & Kubota, H. (1992). Numerical Simulation of Flowfield over a Spiked Blunt Nose. *Computational Fluid Dynamics Journal*, 1(2), 187-195.
16. Boyce, R., Neely, A., Odam, J., & Stewart, B. (2005). CFD Analysis of the HyCAUSE Nose-Cone, AIAA Paper 2005-3339.
17. Milicev, S. S., Pavlovic, M. D., Ristic, S., & Vitic, A. (2002). On the influence of spike shape at supersonic flow past blunt bodies. *Mechanics, Automatic Control and Robotics*, 3(12), 371-382.
18. Mehta, R. C. (2019). Numerical Simulation of Base Pressure and Drag of Space Reentry Capsules at High Speed”, Hypersonic Vehicles - Past, Present and Future Developments, G. Pezzella and A. Viviani, IntechOpen, UK. DOI: 10.5772/intechopen.83651
19. Gauer, M., & Paull, A. (2008). Numerical Investigation of a Spiked Nose Cone at Hypersonic Speeds. *Journal of Spacecraft and Rockets*, 45(3), 459-471.
20. Peyret, R., & Vivind, H. (1993). *Computational Methods for Fluid Flows*, Springer-Verlag, Berlin, 109-111.
21. Jameson, A., Schmidt, W., & Turkel, E. (1981). Numerical Simulation of Euler Equations by Finite Volume Methods Using Runge-Kutta Time Stepping Schemes. AIAA paper 81-1259.
22. Mehta, R. C. (2017). Multi-Block Structured Grid Generation for Computational Fluid Dynamics. *Scholar Journal of Engineering and Technology*, 5(8), 387-219. DOI: 10.21276/sjet
23. Truitt, R. W. (1959). *Hypersonic Aerodynamic*, The Ronald Press Co., New York.
24. Liepmann, H. W., & Roshko, A. (2007). *Elements of Gas Dynamics*, Dover Publications Inc, First South Asian Edition, New Delhi.
25. Shapiro, A. H. (1953). *The Dynamics and Thermodynamics of Compressible Fluid Flow*, John Wiley & Sons.
26. Ames Research Staff, Equations, tables and charts for compressible flow, NACA report 1135, 1953.
27. Hord, R. A. (1955). An approximate solution for axially symmetric flow over a cone with an attached shock-wave, NACA TN 3485.
28. Zumwalt, G. W., & Tang, H. H. (1963). Mach number independence of conical shock pressure coefficient. *AIAA Journal*, 1(12), 2389-2391.
29. Probstein, R. F. (1956). Inviscid flow in the stagnation region of very blunt-nosed bodies at hypersonic flight speeds, WADC –TN 56-395.